X-550-72-268

PREPRINT

NASA TM X-66016

DETERMINATION OF THE GEOID FROM SATELLITE ALTIMETER DATA

SEPTEMBER 1972

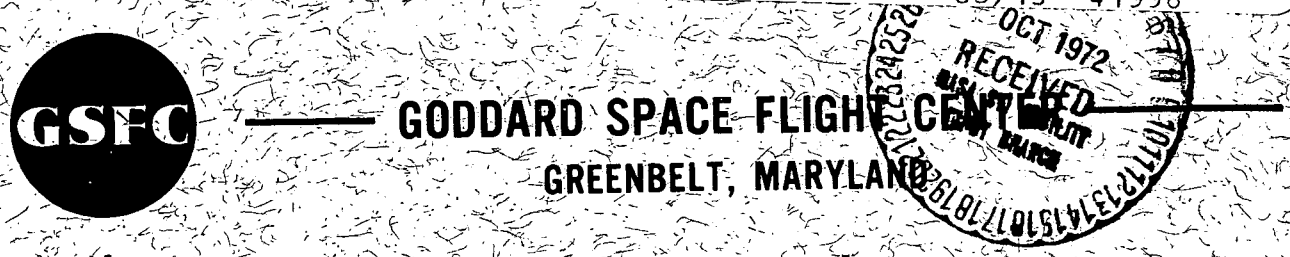

GODDARD SPACE FLIGHT CENTER
GREENBELT, MARYLAND

X-550-72-268

DETERMINATION OF THE GEOID FROM SATELLITE ALTIMETER DATA

R. D. Brown
R. J. Fury
Computer Sciences Corporation

Under
Contract No. NAS5-11790
Task Assignment No. 210

September 1972

GODDARD SPACE FLIGHT CENTER
Greenbelt, Maryland

DETERMINATION OF THE GEOID FROM SATELLITE ALTIMETER DATA

R. D. Brown
R. J. Fury
Computer Sciences Corporation

ABSTRACT

The characteristics of the geoid surface are quantitatively described; a procedure for calculating the satellite altitude is developed; error sources are described quantitatively, mathematically modeled, and evaluated in computer simulation; and procedures for maximum likelihood processing of altimeter data for recovery of orbit and geopotential information are presented for several geopotential models.

CONTENTS

PRECEDING PAGE BLANK NOT FILMED

ILLUSTRATIONS

TABLES

DETERMINATION OF THE GEOID FROM SATELLITE ALTIMETER DATA

SECTION 1

INTRODUCTION

Development of a capability for processing satellite altimeter data has been initiated. This capability will lead to an improved description of the geoid and the geopotential, for which the satellite altimeter is uniquely suited. The surface illuminated by the altimeter can be thought of as a mobile satellite tracking station that travels beneath the satellite and makes range measurements along the local vertical.

In conventional satellite geodesy, a set of fixed tracking stations observe the satellite. From their measurements, the satellite orbital elements, coefficients of the anomalous geopotential model, and station coordinates are recovered in a least-squares adjustment solution. The geoid, one particular surface belonging to a set of equipotential surfaces, is modeled by a reference ellipsoid and a set of geopotential coefficients. The reference ellipsoid is chosen with the use of the station coordinates. A geoid determined in this manner is limited in accuracy and in the level of detail presented due to the generally sparse distribution of tracking stations and the insensitivity of satellite motion to the small geoid features associated with the higher order geopotential coefficients.

Ideally, these limitations do not apply to the use of satellite altimeter data. The effective number of tracking stations can be as large as is necessary, and their distribution is global because they are on the satellite subtrack. In addition, the altimeter measurement is a more direct observation of the geoid height than are other tracking measurements. For example, if the orbit is considered known, then the geoid over ocean regions may be determined directly from these measurements (References 1, 2, and 3). However, the orbit is not completely known because of several factors, such as incomplete and inaccurate force models and tracking system errors. Also, the altimeter measurement is subject to error due both to the instrument and to dynamic sea-surface elevation effects. Orbit error should not degrade the determination of the relative shape of small-scale undulations over fairly long fractional orbit arcs, due to the nearly negligible effect of small-scale geopotential anomalies on the satellite motion (References 2 and 3). However, small-scale anomalies can be expected to influence the orbit over long time periods because of possible resonant conditions between the orbit period and the earth rotation period.

In theory (References 3, 4, 5 and 6), more refined determinations of the geoid can be made by using altimeter data to adjust the geopotential model. This is possible because the mathematical formulations of many geopotential models include parameters that can be related to the spacecraft altitude. Among the geopotential models that were considered are the spherical harmonic expansion (SHE) model, local function models (both orthogonal and non-orthogonal), and models utilizing area-mean free-air gravity anomalies.

The SHE model, is convenient to use because of its universal usage and the orthogonality of its terms. However, a global solution on the fine grid of measurements expected from the altimeter would require the simultaneous solution of a prohibitive number of coefficients.

This requirement for simultaneous solution may be relaxed by using local-function models, generally expressed as mathematical series, each term of which is nonzero only in a particular geographic area. This results in the requirement that only a small subset of the coefficients of a model need be solved simultaneously, constrained only by the existence of altimeter data in the geographic domain of the local functions in question. One local function representation (Reference 4) exhibits its local properties only in difference equation form. The terms of this representation are an orthogonal set and are easily related to spherical harmonics.

Models utilizing surface area-mean gravity anomalies (References 5 and 6) are local with respect to partial sums of the total series expansion. These models are easily converted to SHE formulations and can make use of surface gravity data as well as altimeter data.

An improved geopotential description using any of the above models can lead to a better defined geoid in a bootstrap process by improving knowledge of the orbit (Reference 3). This in turn leads to better geoid determination and a better geopotential model. Altimeter data may also be used directly to help determine the orbit (Reference 3).

At the present state of development of altimetry data processing, the important questions to be considered concern the nature and effect of error sources in the altitude measurement. Although some work (Reference 7) has been done in this area, the questions of the amenability of these errors to filtering techniques, and the requirements to be imposed on the altimeter and its mode of operation in order to realize an improved geoid and geopotential description remain largely unanswered.

The results and conclusions reached to date are summarized in Section 2. Section 3 documents the properties of the surface to be determined, i.e., the geoid. This surface is first described in general; then specific geoid features that are important for the design of the altimeter and altimeter data processing are discussed. The mechanics of the altimeter measurement are presented in Section 4. The influence of the altimeter and spacecraft design on the measurement are described, followed by a mathematical development of the altitude measurement model for simulation purposes. This serves as a background for a discussion of the errors affecting the altimeter measurement in Section 5. Three categories of errors are listed, along with applicable mathematical models. Recent work involving simulation evaluation of the effect of some of these error sources on the derived geoid surface is also presented. A tentative procedure for differential correction of the geoid, geopotential, and orbit parameters is outlined in Appendix A and the specific form of the equations in Appendix A for different geopotential models is presented in Appendix B.

Because of the many symbols used in Sections 3 through 5, a glossary is provided.

SECTION 2

SUMMARY

Some of the first results obtained in connection with developing the capability for processing data from a satellite borne radar altimeter were the description of the characteristics of the geoid surface such as undulation amplitude, scale length, and slopes. These results, valuable in themselves for their implications for altimeter design specifications, enabled the development of a more accurate altitude calculation algorithm, that is, one that considered geoid slopes. Altimeter error sources were also identified and categorized. Mathematical models that were developed to describe the error sources and geopotential models were useful in planning the differential correction process described in Appendices A and B.

Evaluation of the effects of the error sources, as represented by the study of simulated C-band radar tracking data in subsection 5.4, will continue. This will identify those error sources that are important and those that are not and may lead to modifications of the differential correction procedure reported in the appendices. Computer program algorithm based on the mathematical models described in this report are being developed and tested.

SECTION 3

GEOID PROPERTIES

The geoid is an imaginary surface, a particular equipotential surface of the geopotential field. This surface is nearly spherical, with a slight flattening at the poles and a pear-shaped bulge in the southern hemisphere. A finer degree of detail can be deduced from the magnitudes of the higher order terms in a SHE model of the geopotential; this reveals a nonuniform distribution of surface roughness with surface relief on the order of one part in ten thousand. The geoid is approximated closely by a real surface, the sea surface, in ocean areas. The sea surface would conform exactly to the geoid in the absence of currents, tides, and weather-related phenomena (Reference 3). The exact shape of this mean-sea-level (MSL) or marine geoid surface is dictated by the spatial variations in the gravitational potential of the rotating earth. Its shape is important for this study because ideally it is the sea surface that will be defined by the altimeter measurements.

This section examines the properties of the MSL surface, represented by the geoid undulation. Geoid undulation is the deviation of the geoid from the best fitting ellipsoid as measured along the ellipsoid normal. Other properties considered include the horizontal scale length of these deviations, sea slopes, and the importance of these properties for the altimeter measurement.

3.1 Undulation Amplitude

Because the magnitude of the geoid surface relief is very small relative to the earth's radius, a reference surface that closely approximates the geoid is customarily utilized to avoid working with small differences in large numbers. This reference surface, which should be easy to describe mathematically, is usually chosen as the rotationally symmetrical ellipsoid that best fits the geoid, in a least-squares sense, to the accuracy that the geoid is presently known. This surface plays another role in that it represents an equipotential surface of the "normal" potential of the geopotential field. The additional factor (the "disturbing" potential) needed to fully describe the geopotential is thus made small (Reference 9).

The geopotential may be described in geocentric earth-fixed coordinates as

$$W(X, Y, Z) = U(X, Y, Z) + T(X, Y, Z) \qquad (3\text{-}1)$$

where W = the geopotential
U = the normal potential
T = the disturbing potential at the point (X, Y, Z).

To evaluate the magnitude of geoid undulations, one compares the geoid (described by a particular equipotential surface)

$$W(X, Y, Z) = W_0 \tag{3-2}$$

with the reference ellipsoid

$$U(X, Y, Z) = U_0$$

of the same potential

$$U_0 = W_0 \tag{3-3}$$

Following Heiskanen and Moritz (Reference 9) and referring to Figure 3-1, a point P on the geoid is projected along the ellipsoid normal onto point Q on the ellipsoid. This distance PQ, denoted by N, is called the geoidal undulation at P.

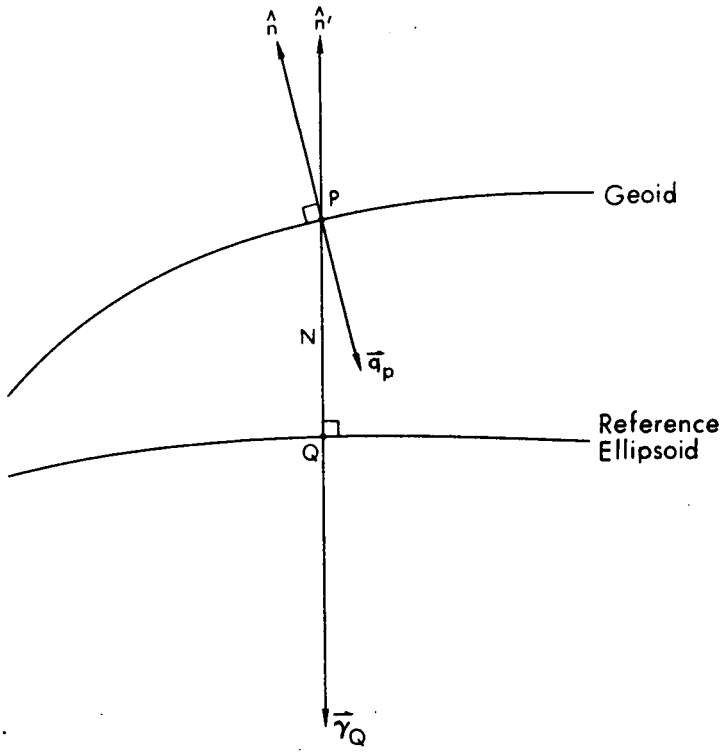

Figure 3-1. Geoid and Reference Ellipsoid

One may approximate the value of the normal potential U at P by a linear relation

$$U_P = U_Q + \left(\frac{\partial U}{\partial \hat{n}}\right)_Q N \triangleq U_Q - \gamma_Q N \tag{3-4a}$$

Since by definition

$$W_P = U_P + T_P \tag{3-4b}$$

and since

$$W_P = W_o = U_Q \tag{3-4c}$$

we find by substituting Equations (3-4c) and (3-4b) into (3-4a) that the geoidal undulation is given by

$$N = \frac{T_P}{\gamma_Q} \tag{3-5}$$

Figure 3-2 (obtained from Reference 10) is a contour map of geoid undulation over the globe as derived from the SAO-M1 geopotential model. This SHE-type model was developed by analyzing satellite tracking data. Note that this geoid consists largely of long-wavelength undulations spanning 20 degrees or more

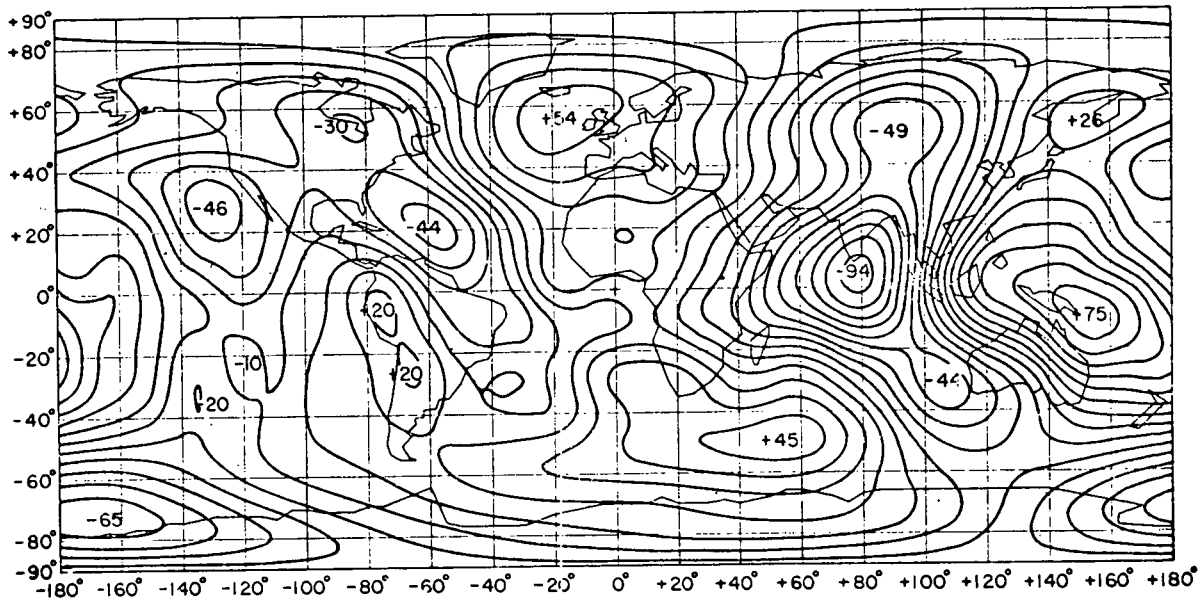

Figure 3-2. Level Curves of Geoid Undulation at 10-Meter Intervals – SAO-M1 Model

in surface distance. This is due to the exclusion of tesseral terms of degree and order larger than 8 in this SHE.* The amplitude of these relatively low-degree undulations is significant, however. The 169-meter (m) range between undulation extremes will be easily sensed by an altimeter of 5-m accuracy. The altitude profiles that might be seen by the altimeter over the SAO-M1 geoid are shown in Figure 3-3. These were generated by overlaying Figure 3-2 with a subtrack of the GEOS-C satellite orbit at 60 degrees inclination for various values of right ascension of the ascending node. A more realistic geoid, that is, one which depicts shorter wavelength undulations, is obtained from the Detailed Geoid Computation (DGC) map (Reference 11) of the Puerto Rico trench area, Figure 3-4. This map was generated from 1-degree area mean gravity anomalies, but height contours have been hand-drawn to a finer scale yielding 6 arc minutes resolution near the trench. Figure 3-5 is a geoid profile derived from Figure 3-4 along the 67th West meridian. Note the sharp change in geoid undulation near 19 degrees North latitude. The 10- to 15-m deviation between the DGC profile and the satellite geoid, drawn here for comparison purposes, shows the difference between a SHE of 8th degree and order for the geopotential and a geopotential model developed from 1° x 1° area means and represents the improvement in geoid determination that can be realized by a direct geoid measurement technique such as satellite altimetry.

3.2 Spectra of Geoid Undulations

A qualitative review of Figures 3-2 through 3-5 reveals that the largest of geoid undulation amplitudes are associated with long-wavelength undulations. This is confirmed by Figure 3-6, which shows the power spectrum of the Puerto Rico trench profile of Figure 3-5. Note the slight peak near the 1-degree wavelength on the Puerto Rico trench spectrum. This is probably due to the trench itself because it is about 1 degree wide in this profile. The overall shape of this curve shows that geoid undulation amplitude decreases rapidly as the wavelength of the feature decreases. If this trend to smaller undulation amplitudes is applicable to the rest of the geoid and if it continues to higher frequencies, then it is unlikely that features (except unusual ones, such as the Puerto Rico trench) of 1-degree wavelength or less will have undulation amplitudes exceeding 2 m.

The shape of geoid spectra have design implications for an altimeter of 1-m precision. To detect geoid undulations whose amplitude is near the 1-m precision limit, the measurement rate of the altimeter according to sampling theory (Reference 12), must be such that at least two measurements per

*More recent SHE models such as the latest GSFC model (Ref. 11) relieve this limitation somewhat in that terms of degree and order 16 are used.

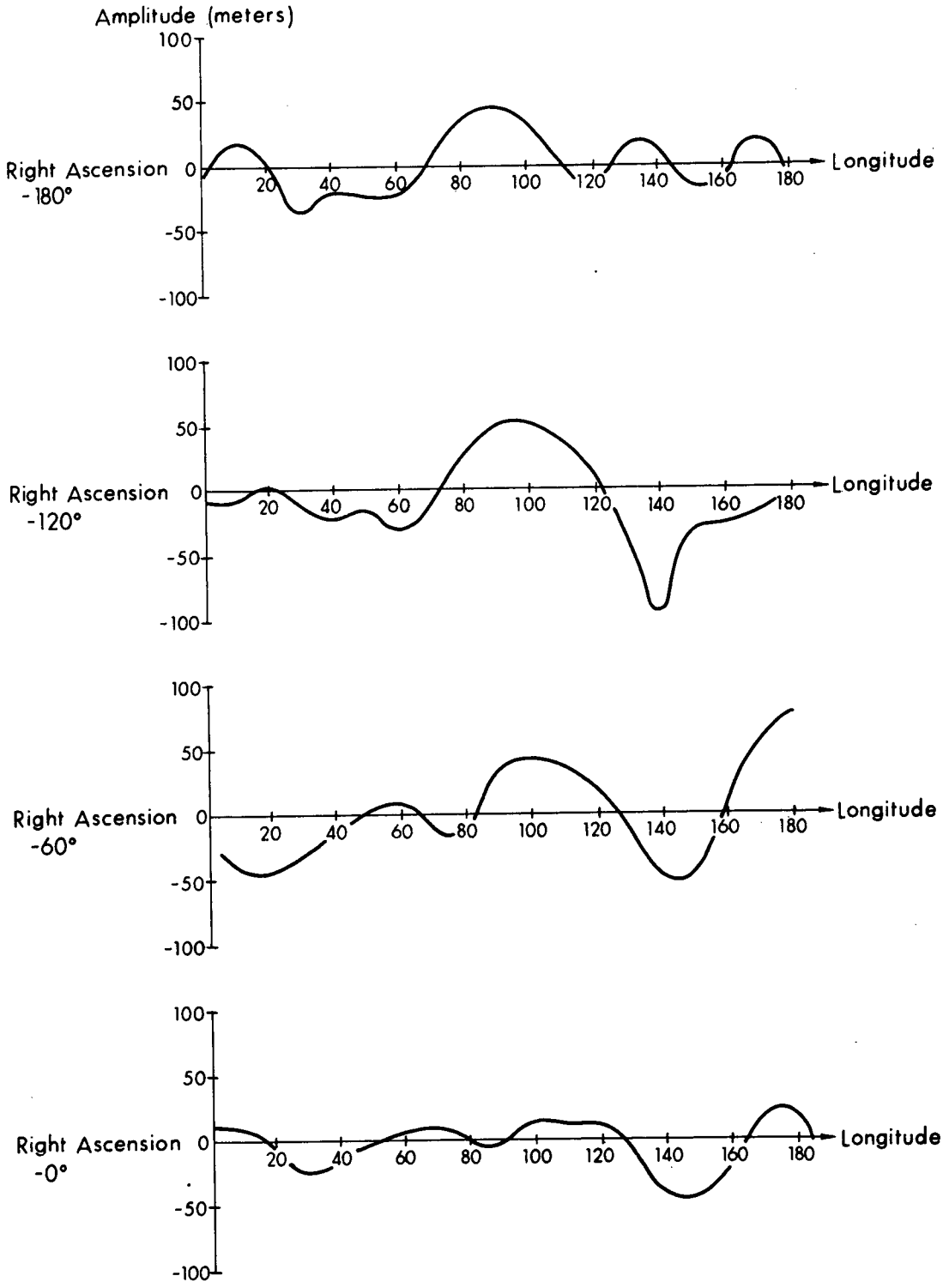

Figure 3-3. SAO-M1 Geoid Profiles

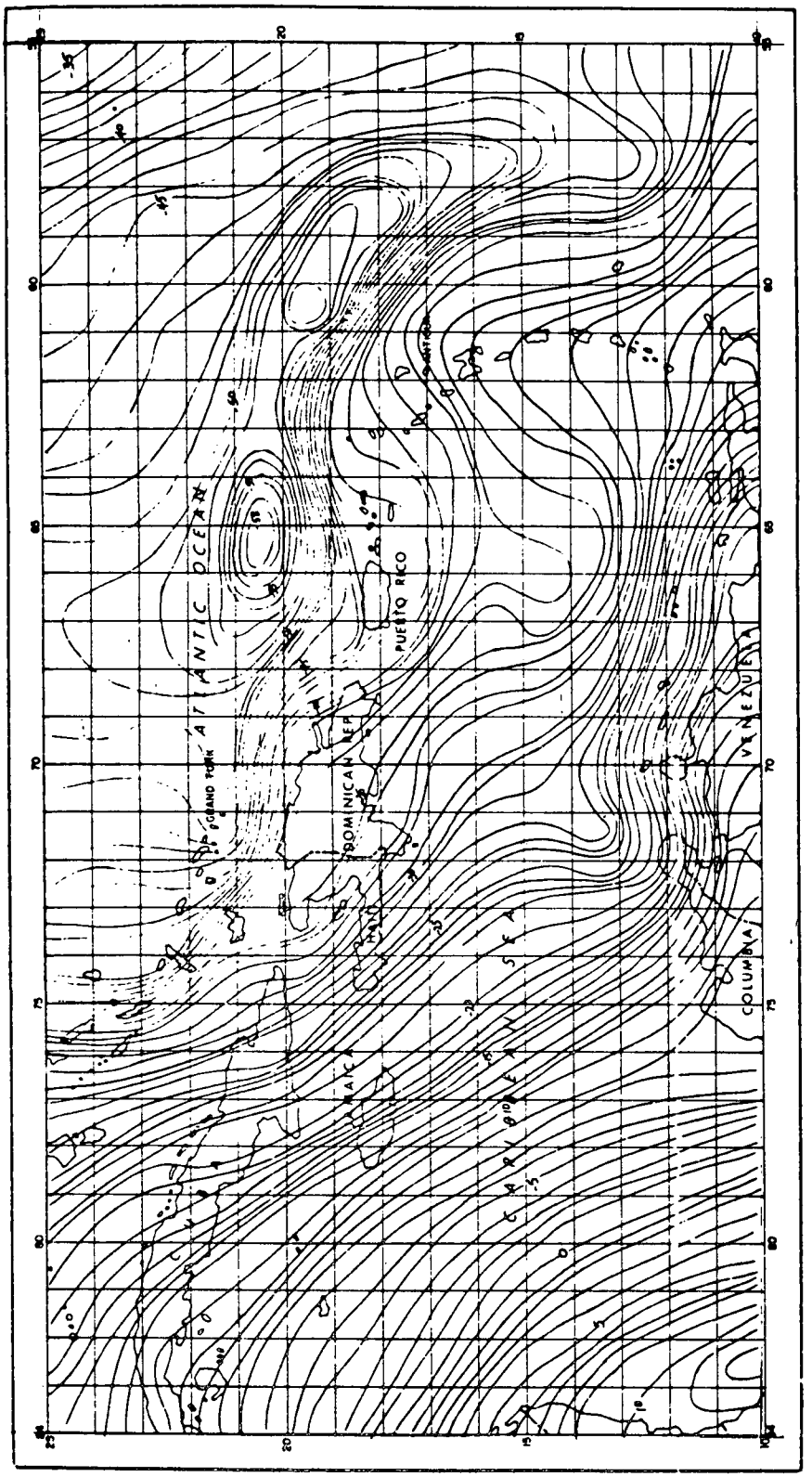

Figure 3-4. Detailed Gravimetric Geoid of the Caribbean

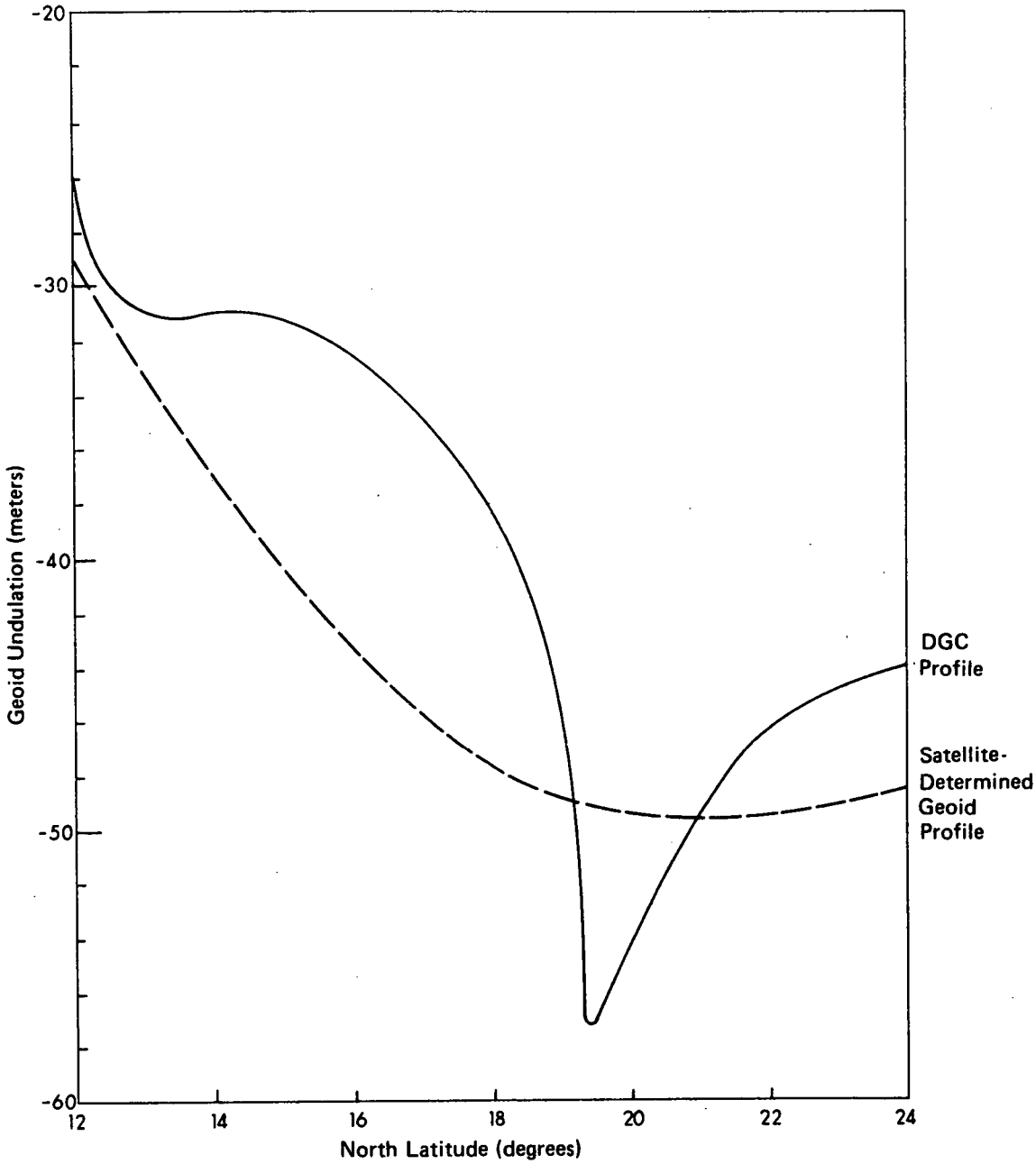

Figure 3-5. Geoid Profile, 67 Degrees West Longitude

undulation wavelength are performed. The current preliminary design sample rate for the GEOS-C altimeter in one operating mode is two per second, which, at the GEOS-C ground speed of nearly 8 kilometers per second (kps), implies that undulation wavelengths smaller than 8 kilometers (km) will not be detected. The adequacy of this sample rate for detecting all undulations of meter amplitude will be reexamined when detailed geoid maps that depict the 8-km undulation wavelength are available.

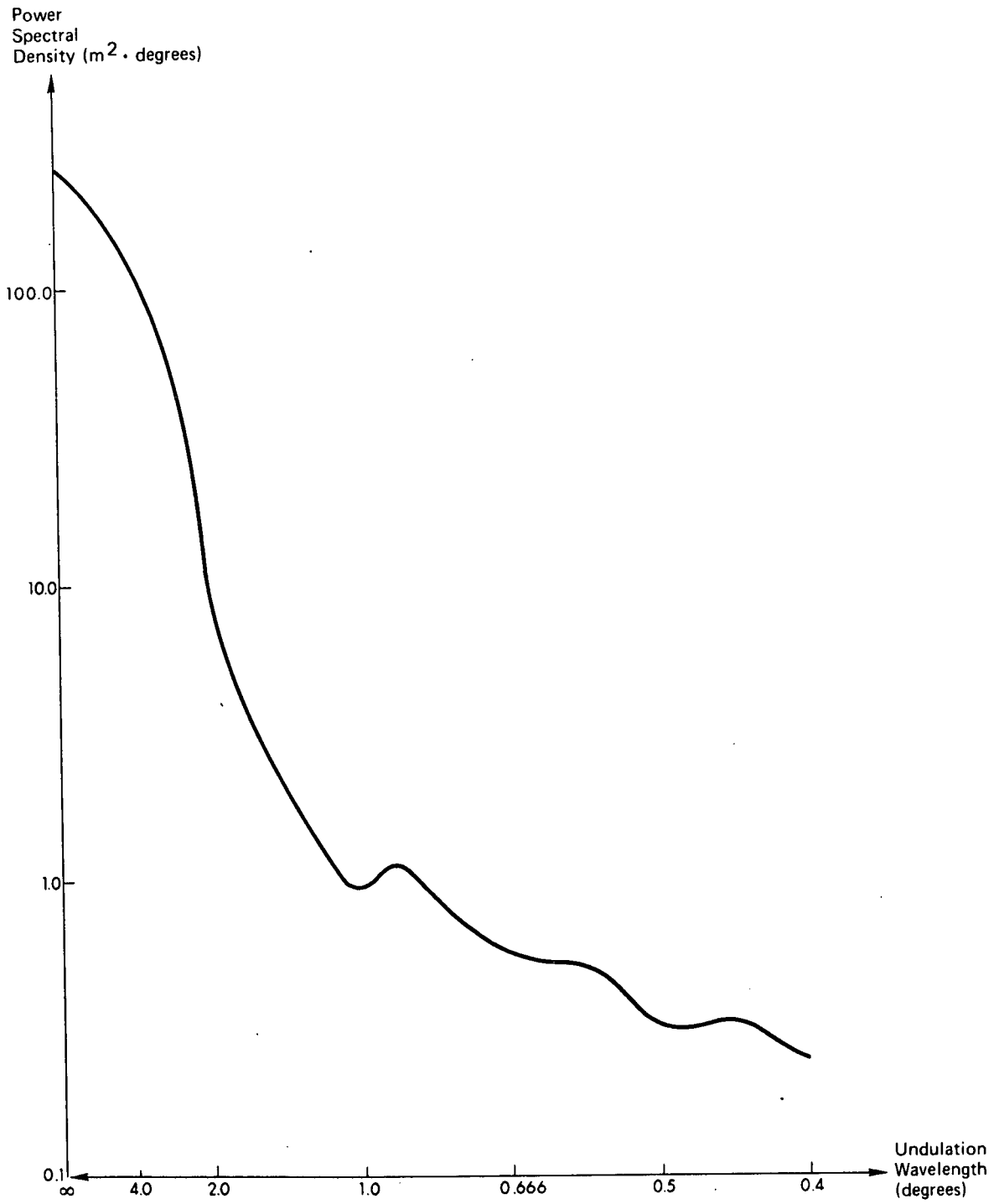

Figure 3-6. Geoid Profile Power Spectra

The detectability of all undulations of one or more meters in amplitude imposes a constraint on the design of the altimeter pulse-width, beam pattern, and return pulse detection process, since all these factors influence the size of the illuminated surface spot. Within the effective illuminated spot, all undulation details are averaged and no information is recovered for wavelengths smaller than the spot diameter. If, as has been proposed (Reference 13), some form of return pulse leading edge detection is used, and the altimeter system is pulse-width limited (see subsection 4.1), then the radius, R_S, of the effective illuminated spot is given in Reference 13 as

$$R_S = \sqrt{c\tau H}\,(\text{km}) \tag{3-6}$$

where

c = the speed of light in kilometers per second
τ = the transmitted radar pulse-width in seconds
H = the satellite altitude (nominal) in kilometers

For $H = 1100$ km and $\tau = 10^{-7}$ sec,

$$R_S = 5.74\,\text{km}.$$

The effective spot diameter is 11.48 km and the effective spot size becomes the limiting factor influencing altimeter horizontal resolution.

3.3 Sea-Surface Slopes

Another geoid property of interest is the local slope of the instantaneous sea surface with respect to the ellipsoid (reference surface). This slope is related to the geoid undulation amplitude and scale length mentioned in subsections 3.1 and 3.2, and needs explicit mention because of its effect upon the altitude measurement. This natural phenomenon will be described here and treated mathematically in Section 4.

The sea surface can assume a slope relative to the reference ellipsoid due to two causes: the geoid (or MSL) slope relative to the ellipsoid (see Figure 3-3) and the departure of the instantaneous sea surface from MSL. A mention of the extremes in sea-surface slopes is sufficient to point out the problems for altimetry.

Slopes due to the disturbance potential are evident in Figure 3-3, which depicts geoid profiles for the SAO-M1 geopotential model. This model, which

describes the long-wavelength geoid undulations, exhibits slopes that range from 0 to 5 m/arc degree, or 4.5×10^{-2} m/km.

On a finer scale, much higher surface slopes can be found in localized areas, such as near the Puerto Rico trench (Figure 3-4). In Figure 3-4, the geoid falls by 11 m over 1 arc degree near 60 degrees West, 18 degrees North. This results in a slope of 9.9×10^{-2} m/km.

Dynamic processes in the ocean, such as tides, barotropic weather effects and long swell waves, generate slopes generally of the same magnitude as those due to the disturbing potential (Reference 3). On the other hand, storm surges, tsunamis, and ocean currents generate a sharp slope at their boundaries. Of these, currents are of more immediate interest because they are of a less transient nature. For example, the Gulf Stream (Figure 3-7) develops a slope on its southeastern edge, due to coriolis acceleration, of 2.26m/arc degree or 2×10^{-2}m/km. Similar slopes can be expected along the edges of other great currents, such as Kuro Shio current.

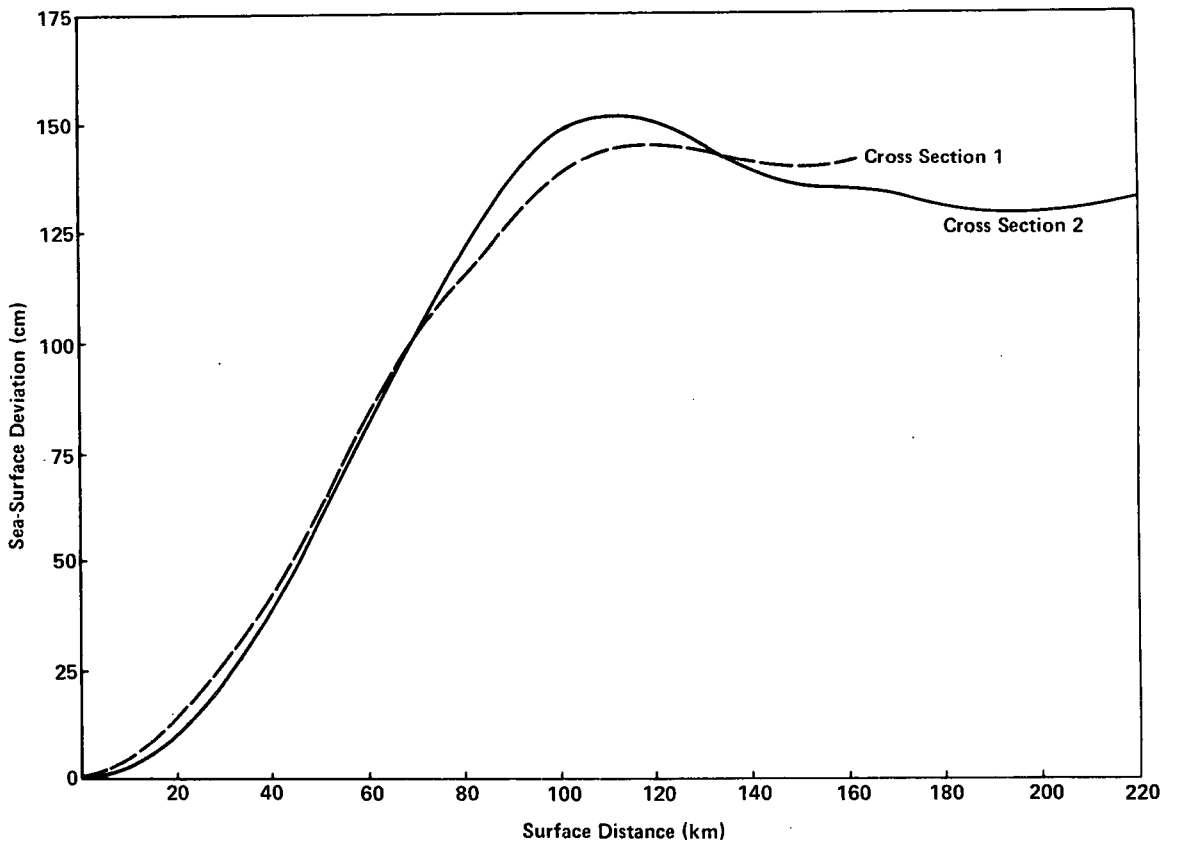

Figure 3-7. Sea Surface Departure from the Geoid Across the Gulf Stream Between 36.5 Degrees North and 38.5 Degrees North Near 68.5 Degrees West (Northern Section) (Reference 3)

SECTION 4

THE ALTIMETER MEASUREMENT

This section describes generally how a satellite altimeter operates, with emphasis on those aspects of the hardware design and operation which constrain the measurement of altitude. A derivation of the calculation of altitude is presented, including a first-order correction to the sea slope.

4.1 Hardware Considerations

The altimeter considered in this section is mounted on a satellite which is gravity-gradient stabilized such that its nominal z-axis lies within a degree or two of the geopotential gradient (local vertical) at the satellite. (See Reference 14 for details of this stabilization mechanism.) Such stabilization allows the use of a directional antenna for the radar altimeter. Figure 4.1, an exaggerated view of the altimeter measurement geometry, shows the spherical shape of the emitted radar wavefront. Because the transmitted beamwidth is larger than the nominal spacecraft libration about the local vertical, the point of first returns from the sea surface will lie on the normal to the sea surface through the satellite, that is, the satellite subpoint. The effective size of the illuminated spot on the surface is determined by the transmitted pulsewidth, the beamwidth, and the type of return pulse detection utilized. A pulsewidth-limited system with leading edge detection will be assumed; the implications of this being that the altitude measurement represents the weighted mean altitude over the surface area illuminated after the leading edge of the pulse intercepts the surface and before the trailing edge does so. This area is significantly smaller than that encompassed by the antenna beam (see subsection 3.2). As mentioned earlier, this imposes a limit of 11.48 km on the horizontal resolution of geoid undulations, for typical values of altitude and pulsewidth.

Another factor that limits the horizontal resolution of the altimeter is the data rate of the instrument. Sampling theory (Reference 12) requires at least two measurements for the shortest wavelength to be detected. The satellite will have a ground speed of nearly 8 km/sec. A data rate of two measurements per second would limit the spectral resolution to 8-km undulation wavelengths, but this limit is superseded by that imposed by the effective spot size.

The configuration presented by the satellite antenna offers some protection against the libration of the satellite. The antenna beamwidth half angle is 1.3° which subtends a spot of 45.2 km diameter at the surface. As long as the satellite effective illuminated area lies inside the beamwidth spot, i.e. the satellite z-axis intersects the sea surface at a point at least 5.74 km inside the antenna

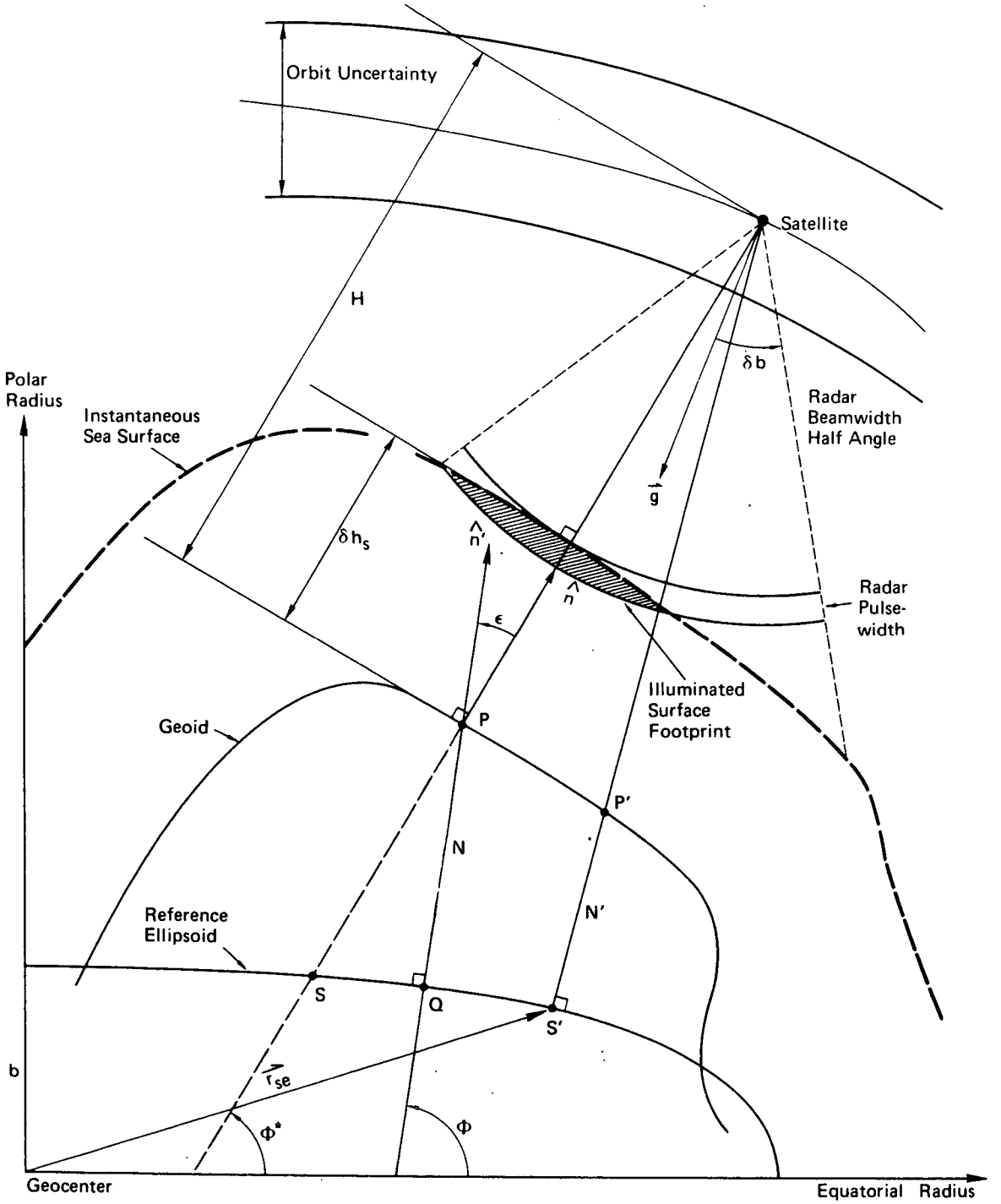

Note: Refer to the Glossary for Definitions of Symbols.

Figure 4-1. Altimeter Measurement Geometry

beamwidth cone at the surface, the altimeter measurement will represent the shortest distance between the satellite and the sea surface. When satellite libration exceeds this limit, the altimeter measurement no longer represents the true altitude and sophisticated error-correcting models and procedures must be employed.

4.2 Measurement Geometry

Because the altimeter measurement is nominally the shortest distance between the satellite and the sea surface, the measurement is along the normal to the sea surface that passes through the satellite. Although this direction is not generally parallel to the ellipsoid normal at that point (see subsection 3.3 and Figure 4-1), it is close enough for a zero-order approximation to assume that the ellipsoid normal is the measurement direction. At the satellite, the z-axis is controlled to the local vertical. Because equipotential surfaces at satellite altitude are even closer approximations to an ellipsoid, this local vertical can also be assumed to be the normal to an ellipsoidal surface. However, this normal is not generally the same as the reference ellipsoid normal due to curvature of the gradient of the normal potential.

Assuming that the measurement is made along the ellipsoid normal at S', the factors that influence the error in the measured altitude are represented in Figure 4-1. The geoid differs from the ellipsoid both in distance and in slope, and, to a lesser extent, the sea surface itself differs from the geoid in the same manner. The geoid undulation, N, is the unknown parameter to be solved for, but its determination is made difficult by the slope of the sea surface relative to the ellipsoid, the deviation of the sea surface relative to the geoid, the less-than-perfect knowledge of the geoid, and the uncertainty in the satellite position (orbit uncertainty).

4.3 Calculated Altitude

To simulate the altitude measurement, it is necessary to calculate a number that in theory represents the actual altitude. This capability is also needed when forming altitude residuals, that is, the difference between observed and calculated altitudes, for least-squares differential correction of geoid and geopotential parameters. The calculation of altitude is accomplished herein by an iterative procedure.

Figure 4-1 shows the antenna of a spacecraft-borne altimeter sensor system that is oriented in the direction of the gravity acceleration vector $(\vec{g})$ at the satellite, assuming a gravity-gradient stabilized sensor platform. The height of the satellite is measured in the direction of shortest signal echo, which is along the

normal to the instantaneous sea surface. This direction is very close to the local normal, $\hat{n}$, to the geoid (i.e. the direction of line segment SP), especially over ocean areas. The separation of geoid and ellipsoid at P and Q, respectively, along the ellipsoidal normal, $\hat{n}'$, is defined as the geoid undulation, N.

Ideally, the satellite altitude at P should be calculated along the line from P to the satellite, of distance H. However, the location of point P is unknown, so approximate techniques are used. Although N does not coincide with the SP line segment, the height of the satellite above the ellipsoid may be approximated initially as

$$h = H + N \tag{4-1}$$

where H = the satellite height above the geoid at P. The coordinates of point Q are also generally unknown. Thus both H and N are unknown. We must have an approximation to h in terms of known parameters. This approximation is developed in the following sections.

The position of the spacecraft with respect to the geocentric coordinate system (Figure 4-2) is determined at any given time from the dynamics of the system and the estimated state vector. Because the satellite height is a scalar quantity, it is immaterial whether the coordinate system is inertial or earth fixed. However, for the definition of geopotential, it is assumed to be earth fixed and Greenwich oriented. The geocentric spherical coordinates of the spacecraft are as follows:

$$\begin{aligned} \Psi &= \mathrm{Tan}^{-1}\left[\frac{Z_e}{\left(X_e^2 + Y_e^2\right)^{\frac{1}{2}}}\right] \\ \Omega &= \mathrm{Tan}^{-1}\left[\frac{Y_e}{X_e}\right] \\ r_e &= \left(X_e^2 + Y_e^2 + Z_e^2\right)^{\frac{1}{2}} \end{aligned} \tag{4-2}$$

These coordinates can be used to calculate the distance between the satellite and the ellipsoid at closest approach, that is, point S'.

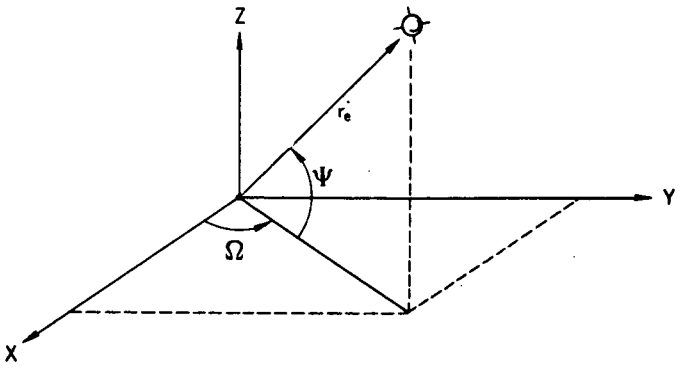

Figure 4-2. Geocentric Spherical Coordinates

The actual height of the satellite above the ellipsoid at S' along the ellipsoidal normal is (see Figure 4-3) given by

$$h' = \frac{\sqrt{X_e^2 + Y_e^2}}{\cos \phi} - r_N \tag{4-3}$$

where X_e, Y_e = satellite geocentric coordinates
ϕ = the geodetic latitude of S'
r_N = the normal radius of curvature of the ellipsoid at S'
This expression for h' is the desired zero-order approximation to h.

To implement Equation (4-3), one must express r_N and ϕ in terms of measured or known parameters. According to Bomford (Reference 15), the radius of curvature, r_N, of the ellipsoid at S' is given by

$$r_N = \frac{a}{\left[1 - (2f - f^2) \sin^2 \phi\right]^{\frac{1}{2}}} \tag{4-4}$$

where a = the semimajor axis of the ellipsoid and
f = the ellipsoid flattening, both known parameters.

Therefore, the implementation of Equation (4-3) depends only on the determination of the angle ϕ. This angle cannot be calculated in closed form (Reference 9). An iterative solution is possible, however, starting with the known satellite coordinates and assuming that h' is initially negligible.

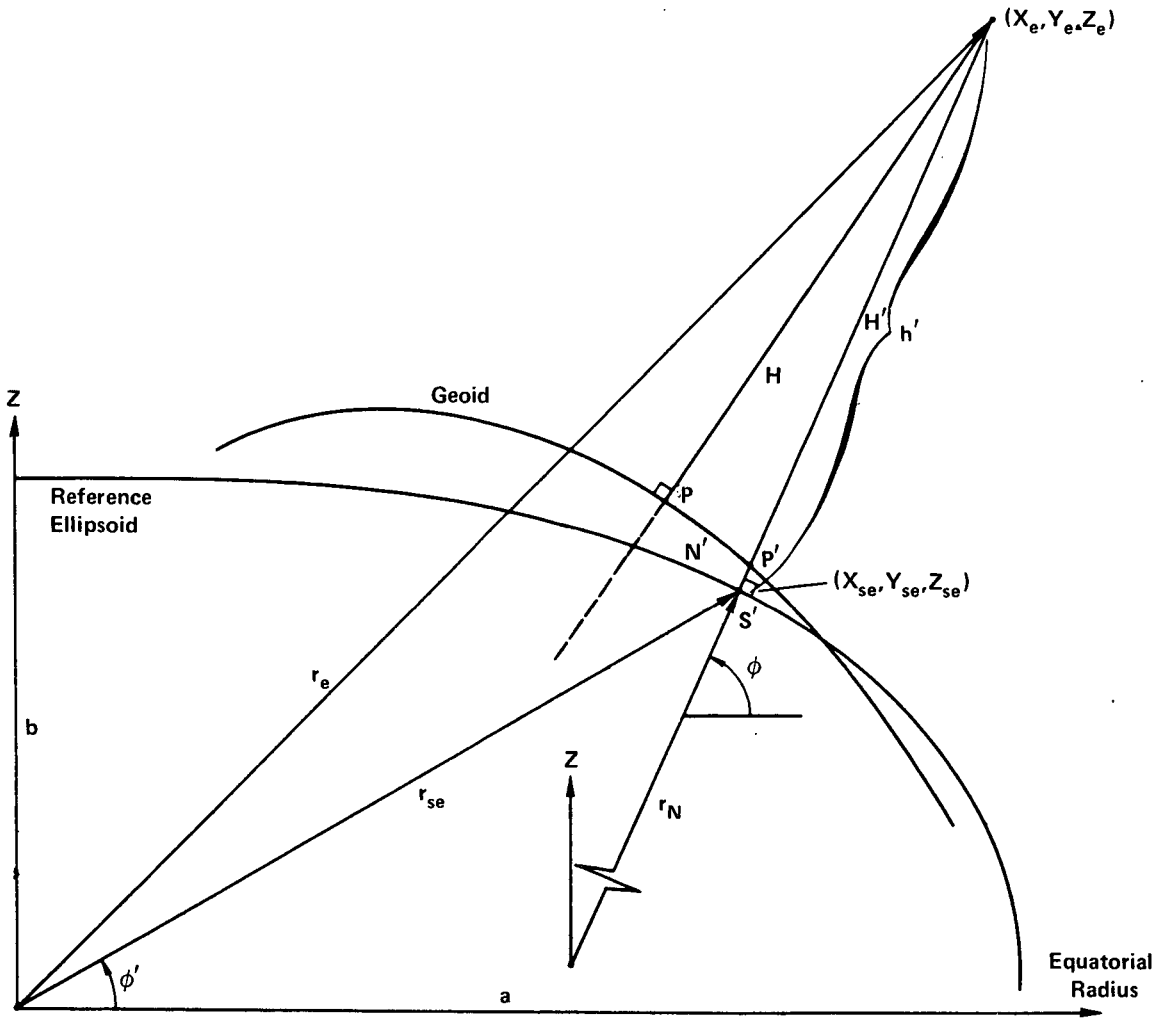

Figure 4-3. Reference Ellipse Measurement Geometry

From Equation (4-3) we may write

$$\sqrt{X_e^2 + Y_e^2} = (r_N + h') \cos \phi \qquad (4\text{-}5)$$

From Bomford (Reference 15),

$$Z_e = \left\{ \left[1 - (2f - f^2) \right] r_N + h' \right\} \sin \phi \qquad (4\text{-}6)$$

Forming the fraction and reducing we obtain

$$\tan \phi = \frac{Z_e}{\sqrt{X_e^2 + Y_e^2}} \left[1 - (2f - f^2) \frac{r_N}{r_N + h'} \right]^{-1} \qquad (4\text{-}7)$$

Setting $h' = 0$ in Equation (4-7), the first approximation to ϕ is obtained

$$\phi_1 = \tan^{-1} \left\{ \frac{Z_e}{\sqrt{X_e^2 + Y_e^2}} \left[(1 - 2f + f^2) \right]^{-1} \right\}$$

This value for ϕ is substituted into Equation (4-4), where r_{N_1} is evaluated. This in turn enables us to approximate h' using Equation (4-3).

$$h'_1 = \frac{\sqrt{X_e^2 + Y_e^2}}{\cos \phi_1} - r_{N_1} \qquad (4\text{-}8)$$

A second approximation for ϕ, denoted ϕ_2, may now be computed from Equation 4-7, that is

$$\phi_2 = \tan^{-1} \frac{Z_e}{\sqrt{X_e^2 + Y_e^2}} \left[1 - (2f - f^2) \frac{r_{N_1}}{r_{N_1} + h'_1} \right]^{-1} \qquad (4\text{-}9)$$

and so on, until ϕ_i and h'_i converge.

The zero-order approximation to the measured altitude is therefore (see Figure 4-3)

$$H' - \delta h'_s = h' - N' - \delta h'_s$$

where $\delta h'_s$ = the deviation of the sea surface from the geoid at S' (see Figure 4-1)

N' = the geoid undulation at S'.

The geoid undulation N' at the point S' is given by Equation (3-5) as

$$N' (\phi', \lambda) = \frac{W - U}{\gamma}$$

where $W = W(r_{se}, \phi', \lambda)$ is the estimated potential S'
$U = U(r_{se}, \phi', \lambda)$ is the normal potential S'
r_{se} = the geocentric radius to S'
λ = the longitude of S'
ϕ' = the geocentric latitude at S'
γ = the gradient of U at S'
These parameters must also be evaluated in terms of known parameters.

The gradient, γ, is given by Heiskanen and Moritz (Reference 9) as

$$\gamma = \gamma_e \left(1 + f_2 \sin^2 \phi + f_4 \sin^4 \phi\right)$$

where $f_2 = -f + \frac{5}{2}m + \frac{1}{2}f^2 - \frac{26}{7}fm + \frac{15}{4}m^2$

$$f_4 = -\frac{1}{2}f^2 + \frac{5}{2}fm$$

$$m + \frac{3}{2}m^2 \cong \frac{\omega^2 a}{\gamma_e} \quad (\omega \text{ is the rotation rate of earth})$$

Further,

$$\gamma_e \cong 978.049 \text{ gal}$$

$$\omega \cong 0.72921151 \times 10^{-4} \text{ rad/sec}$$

The value of m may be obtained by an iterative process from

$$m_n = \frac{\omega^2 a}{\gamma_e} - \frac{3}{2} m_{n-1}^2 \qquad \text{for } n = 1, 2, \ldots$$

and

$$m_o = 0.00344986$$

The geocentric radius r_{se} and latitude ϕ' may be evaluated from

$$r_{se} = r_N \left[1 - \sin^2 \phi \,(4f - 6f^2 + 4f^3 - f^4)\right]^{\frac{1}{2}}$$

and

$$\phi' = \tan^{-1}\left\{\left[1-(2f-f^2)\right]\tan\phi\right\} \quad \text{(Reference 15)} \tag{4-10}$$

To this point we have detailed the derivation of a zero order approximation to the altitude measurement by calculating the altitude to P'. This derivation assumes negligible surface slope between P and P'. Figure 4-3 illustrates the effect of geoid slope on the altitude calculation. The difference between H at P and H' at P' shows the need for a better approximation to the actual altitude H above the geoid at P. If one assumes a first-order or planar approximation to the geoid slope, the discrepancy between H and H' is found to be as much as 2.24 m for the geoid slope values presented in subsection 3.3. For example, from the geometry of Figure 4-4,

$$|H - H'| = (H \tan \delta_b)(\tan \epsilon)$$

where $(\tan \epsilon)$: The geoid slope in meters per meter surface distance

If δ_b = 1.3 degrees
H = 10^3 km
and $\tan \epsilon = 9.9 \times 10^{-5}$ m/m then

$$\left|H - H'\right|_{MAX} = 2.24 \text{ m}$$

To implement the first order approximation one must first estimate the coordinates of P. This requires an estimate of the coordinates of Q and an evaluation of geoid slope.

Geoid slope is expressed by the angle difference (ϵ) between the geoidal and ellipsoidal normals, called deflection of the vertical. The components of ϵ at P in the meridian and prime vertical planes are ξ and η, respectively, and are calculated through the partial differentials of geoid undulation as formulated by Vening Meinesz (Reference 9).

$$\xi = -\frac{1}{R}\frac{\partial N}{\partial \Phi}$$

$$\eta = -\frac{1}{R\cos\Phi}\frac{\partial N}{\partial \Omega}.$$

where

$$\epsilon = (\xi^2 + \eta^2)^{\frac{1}{2}} \tag{4-11}$$

$$R = a\sqrt[3]{1-f}$$

Note that Φ is the geodetic latitude of Q.

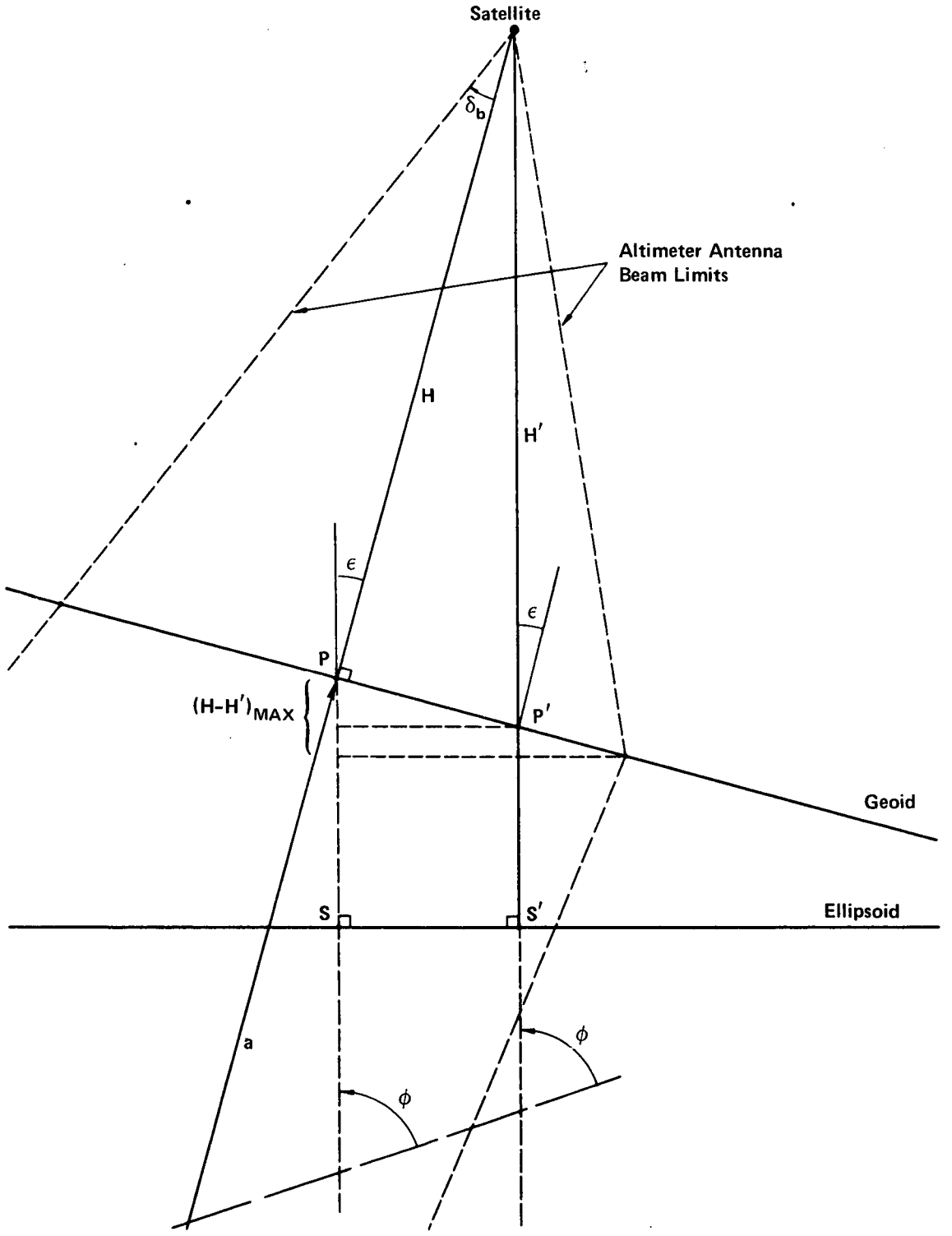

Figure 4-4. Radar Beam – Surface Geometry

If one knows the geodetic coordinates of point Q (see Figure 4-1), that is, Φ and Ω, then one can calculate the astronomical coordinates Φ^*, Ω^* (see Figure 4-1) of P by means of

$$\Phi^* = \Phi + \xi$$

and

$$\Omega^* = \Omega + \frac{\eta}{\cos \Phi}$$

The expressions for the deflection of the vertical depend upon the mathematical form of the geopotential models. If the geopotential at P is modeled by a SHE, then the disturbing potential at P may be expressed as

$$T_P = \frac{GM}{r} \sum_{n=2}^{L^*} \left(\frac{a}{r}\right)^n \sum_{m=0}^{n} \left(C_{nm} \cos m\Omega + S_{nm} \sin m\Omega\right) P_{nm}(\sin \phi') \quad (4\text{-}12)$$

where GM is the gravitational constant of the earth

C_{nm}, S_{nm} are SHE coefficients

$P_{nm}(\sin \phi')$ are associated Legendre functions

L^* indicates that the terms with n=2, m=0, n=4, and m=0 are deleted from the summation (Reference 9), and the geocentric radius to P, denoted by r, is approximated by

$$r = r_{se} + N' \quad (4\text{-}13)$$

The geoid undulation N' may be approximated using Brun's formula (Equation 3-5) and Equation (4-12). Replacing $\partial/\partial\Phi$ by $\partial/\partial\phi'$, one obtains upon substitution into Equation (4-11),

$$\xi = -\frac{1}{\gamma R} \frac{GM}{r} \sum_{n=2}^{L^*} \left(\frac{a}{r}\right)^n \sum_{m=0}^{n} \left(C_{nm} \cos m\Omega + S_{nm} \sin m\Omega\right) \frac{dP_{nm}(\sin \phi')}{d\phi'} \quad (4\text{-}14)$$

and

$$\eta = \frac{1}{\gamma R \cos \phi'} \frac{GM}{r} \sum_{n=2}^{L^*} \left(\frac{a}{r}\right)^n \sum_{m=0}^{n} m \left(C_{nm} \sin m\Omega - S_{nm} \cos m\Omega\right) P_{nm}(\sin \phi') \quad (4\text{-}14)$$

where the partial with respect to γ is ignored as being of second order

then

$$\frac{dP_{nm}(\sin\phi')}{d\phi'} = -\frac{n}{\cos\phi'}\left[\sin\phi' P_{nm}(\sin\phi') - P_{n-1,\,m}(\sin\phi')\right] \text{ for } m=0, \text{ and}$$

$$\frac{dP_{nm}(\sin\phi')}{d\phi'} = m\frac{\sin\phi'}{\cos\phi'}P_{nm}(\sin\phi') - (n+m)(n-m+1)P_{n,\,m-1}(\sin\phi')$$

for $m \neq 0$.

The geocentric rectangular coordinates of the satellite i.e. X_e, Y_e, Z_e, are assumed to be known. Therefore, ϕ, ϕ', and λ can be computed directly from Equations (4-6) through (4-10). The coordinates of P and Q, i.e. the angles Φ and Ω and $\Phi^*$and Ω^*, are yet unknown. If, as in Figure 4-4, the ellipsoid and geoid are assumed to be planar within the area subtended by the altimeter antenna beam, then

$$\Phi = \phi$$

and

$$\Omega = \lambda$$

The deflection of the vertical at P' is now the same as at P and the coordinates of P (Φ^*, Ω^*) may be calculated with the use of Equations 4-11 through 4-14.

Knowledge of the coordinates of P permits better approximation to the calculated height above the ellipsoid. The direction cosines of the local vertical at P are

$$\begin{aligned} \cos\alpha &= \cos\Phi^*\cos\Omega^* \\ \cos\beta &= \cos\Phi^*\sin\Omega^* \\ \cos\gamma &= \sin\Phi^* \end{aligned} \qquad (4\text{-}15)$$

This is the direction of the true altitude measurement, assuming first-order (planar) corrections to the geoid slope. One can now solve for the first-order approximate height, h, above the ellipsoid. The equations of ellipsoid and the local vertical are

$$b^2X^2 + b^2Y^2 + a^2Z^2 = a^2b^2 \qquad (4\text{-}16)$$

$$X = \frac{\cos \alpha}{\cos \gamma} (Z - Z_e) + X_e \tag{4-17}$$

$$Y = \frac{\cos \beta}{\cos \gamma} (Z - Z_e) + Y_e \tag{4-18}$$

where b is the semi-minor axis of the reference ellipsoid.

The simultaneous solution of Equations (4-16) through (4-18) for the z coordinate gives

$$Z = \frac{-b^2 (A+B) \pm \left\{ b^4 (A+B)^2 - 4\left[a^2 + b^2(Q^2+P^2)\right]\left[b^2 (C+D-a^2)\right] \right\}^{\frac{1}{2}}}{2\left[a^2 + b^2(Q^2+P^2)\right]} \tag{4-19}$$

where $A = 2Q(X_e - Q Z_e)$

$B = 2P(Y_e - P Z_e)$

$C = (QZ_e - X_e)^2$

$D = (PZ_e - Y_e)^2$

$Q = \cos \alpha / \cos \gamma$

$P = \cos \beta / \cos \gamma$

The correct solution of Equation (4-19) has the same sign as Z_e. Finally

$$h = \left[(X_e - X)^2 + (Y_e - Y)^2 + (Z_e - Z)^2 \right]^{\frac{1}{2}}$$

The calculated altitude measurement to the sea surface is thus

$$H - \delta h_s = h - N(\Phi, \Omega, r) - \delta h_s \tag{4-20}$$

where δh_s = the deviation of the sea surface from the geoid at P.

SECTION 5

ERROR SOURCES

The error sources that affect the estimate of the geocentric radius to the geoid at the measurement point are of three types: those that contribute to uncertainty in the geocentric distance to the satellite, those that cause the measured surface to deviate from the true geoid, and those that affect the accuracy of the measurement itself. In the sections that follow, the dominant error sources (i.e., those that contribute errors larger than about 10 centimeters (cm) in each category) are identified.* Most of these sources may be modeled by mathematical formulae whose parameters are adjustable in a least-squares differential correction procedure (see Appendix A). A few sources may be treated by selective filtering matched to their error spectra.

After identification of the sources, their characteristics and mathematical models are discussed, followed by an evaluation of their effects. Error models developed herein are accurate to first order: second order effects such as earth curvature are neglected. Note that although GEOS-C satellite mission parameters are used frequently as an example, the error model characteristics are general for all near-earth satellite altimeter missions. Additional error sources may exist for a particular mission or a particular altimeter design but the characteristics of these sources are not sufficiently well known at this time to allow their discussion in this report.

5.1 Orbit Errors

In general, the geocentric geoid radius is determined by the difference between the geocentric satellite radius and the altimeter measurement. Any orbit error that causes a radial deviation from the expected trajectory will show up directly in the calculated geoid radius, or in the derived geoid undulation.

Table 5-1 lists the factors that can cause more than 10 cm of error in the predicted satellite radius. All these sources are currently modeled and implemented in general orbit prediction programs, such as NONAME, GEOSTAR, and NAP. The correction magnitude needed represents the importance of the error source, not the uncertainty in altitude after correction of a particular error.

*This choice of error threshold assumes a nominal altimeter measurement precision of ±1 m.

Table 5-1

Order of Magnitude of Expected Altitude Corrections

SOURCE	TYPICAL MAGNITUDE CORRECTION NEEDED
TROPOSPHERIC REFRACTION	2 M (REFERENCE 17)
IONOSPHERIC REFRACTIVITY AND REFRACTION	10 CM[a]
TROPOSPHERIC REFRACTIVITY	1 M
TRACKING STATION POSITION ERROR	10 M (REFERENCE 10)
MEASUREMENT BIAS	10 M (REFERENCE 7)
TIMING BIAS	10 M
PHASE ANGLE ERROR (FOR PHASE SYNCHRONOUS TRACKING SYSTEMS)	10 M
MEASUREMENT SCALE ERROR	1 M
DYNAMIC MEASUREMENT TIME LAG	10 CM
ATMOSPHERIC DRAG	1 CM[b] TO 1 KM
SOLAR WIND	1 CM[b] TO 1 KM
GEOPOTENTIAL ERROR	20 M (REFERENCE 7)

[a] DEPENDS ON TYPE OF MEASUREMENT.

[b] DEPENDS ON ARC LENGTH, SATELLITE, AND ALTITUDE.

These numbers depend very much on the type of tracking system used. For example, a laser tracking system that may suffer a 1-m error due to ray path bending in the troposphere (see Ref. 18, pp. 21-23) is completely unaffected by the ionosphere. On the other hand, Doppler tracking usually incorporates a built-in correction for ionospheric effects, and resulting ionospheric errors are on the order of centimeters.

Tropospheric refraction is the time delay experienced by electromagnetic signals due to the greater-than-unity value of the tropospheric index of refraction. As mentioned earlier, refractivity refers to ray path bending. The amount of bending (and the consequent range error) varies with radio frequency. Tracking station position error is mislocation of the station in the

geocentric coordinate system. Measurement bias is merely a calibration error in the tracking system. Constant error in the estimate of the time of the measurement is called timing bias. Phase-angle error is analogous to a measurement bias for such systems as Minitrack that rely on measurement of phase angle. Scale error is an error whose magnitude is proportional to the magnitude of the measurement. Dynamic measurement time lag refers to the satellite's change in position between the time that the tracking signal is sent and the time that the measurement information is received at the station. The radial position error due to dynamic time lag is proportional to satellite radial acceleration. Atmospheric drag tends to cause a secular decrease in the value of satellite apogee (and orbit radius) leading eventually to atmosphere reentry of the satellite. Solar wind is a periodic force (once per satellite revolution) leading to changes in orbit eccentricity and hence a change in satellite orbit radius at both apogee and perigee. Both of these sources of radial error are included in the force model of the general orbit prediction programs and are included in the corresponding least-squares correction process. Error in the geopotential can cause both short- and long-term radial errors, although the dominant frequency involved appears to be that of the revolution of the satellite about the earth (Reference 7).

The model for tropospheric refraction is in the form of a correction to the measurement. For example, for range, ρ, the correction due to refraction (Reference 16) is

$$\Delta\rho = \frac{2r_s (n_s - 1)^2 \left[1 + n_s \frac{\ell^2}{4(n_s - 1)} \right]}{\sin E + (\ell^2 + \sin^2 E)^{\frac{1}{2}}} \text{ (meters)} \qquad (5\text{-}1)$$

where r_s = the geocentric radius to the station

n_s = the index of refraction

$\ell^2 = 28800/r_s$

E = the elevation angle of the ray path from the station to the satellite.

Other more sophisticated models for tropospheric refraction correction such as that by Hopfield (Reference 18) may also be used.

Refractivity correction can be implemented by means of a correction to the elevation angle as follows (Reference 16),

$$\Delta E = \frac{2 (n_s - 1) \cos E}{\sin E + (\ell^2 + \sin E)} \text{ (radians)} \qquad (5\text{-}2)$$

The models for ionospheric effects are similar in form to Equations (5-1) and (5-2), for a fixed frequency tracking signal.

Corrections to range measurements due to other sources are modeled (Reference 16) as

$$\delta\rho = \rho_{x_s} B_E + \rho_{y_s} B_N + \rho_{z_s} B_U + B + \dot{\rho} T + \Delta\rho_{rf} R + \tau \mathfrak{D} + \rho S + \ddot{\rho} L \tag{5-3}$$

where $\rho_{x_s}, \rho_{y_s}, \rho_{z_s}$ = the partial derivatives of range with respect to the components of tracking station error X_s, Y_s, Z_s

B_E, B_N, B_U = the coefficients of tracking station error in the East, North, and vertical (up) directions

B = the measurement bias coefficient

$\dot{\rho}$ = the time rate of change of range

T = the coefficient of the timing bias error model

$\Delta\rho_{rf}$ = the specific ionospheric refraction correction

R = the coefficient of the ionospheric refraction

τ = the model for specific phase error

$\mathfrak{D}$ = the phase-error model coefficient

S = the coefficient of the range scale-length error model

L = the coefficient of the range dynamic lag error model

An evaluation of the effect of some of these error models is presented in subsection 5.4.

In the Network Analysis Program (NAP) general orbit prediction (Reference 16), atmospheric drag, solar wind, and geopotential effects are all evaluated in a differential correction process in accordance with the mathematical models described in Reference 16. The effect of error in the geopotential model, illustrating the situation in which geopotential correction is not applied, is depicted by Marsh and Douglas (Reference 7). An error in spherical harmonic coefficients of the difference between coefficients of two contemporary SHE geopotential models was simulated and its effect on a typical GEOS-C satellite orbit was plotted. Radial errors in orbit prediction of 20-m amplitude with a period equal to the orbital revolution resulted. This indicates that when the geopotential error is merely modeled without differential correction, the effective error in radial orbit prediction may be removed from the altimeter measurement residuals by a filter set at the satellite revolution frequency.

The effect of small-scale anomalies in the geopotential, such as the Puerto Rico trench, are typically not modeled by SHE models. This trench causes a perturbation of about 200 milligals (mgal) in surface gravity acceleration over an area 1 degree wide and 8 degrees long. To study the effect of such anomalies on the radial component of the GEOS-C orbit, a concentrated mass (mascon) was located at a depth of 100 km and its effect on the orbit was simulated in the NO-NAME orbit prediction program. The magnitude of the mass was chosen to yield the observed surface gravity anomaly (Reference 11). The short-term effect on the radial component of the orbit is negligible compared to the 20 m error due to uncertainty in lower degree and order terms of the geopotential SHE. The radial deviation of the orbit from the nominal orbit is plotted in Figure 5-1. The true effect of the local anomaly is evident within minutes of the time of closest approach to the mass concentration. The long-period phenomenon, with a frequency equal to the satellite revolution, is erroneous and is due to the aliasing of the effect of the added mass with the low-order zonal terms of the SHE geopotential model.

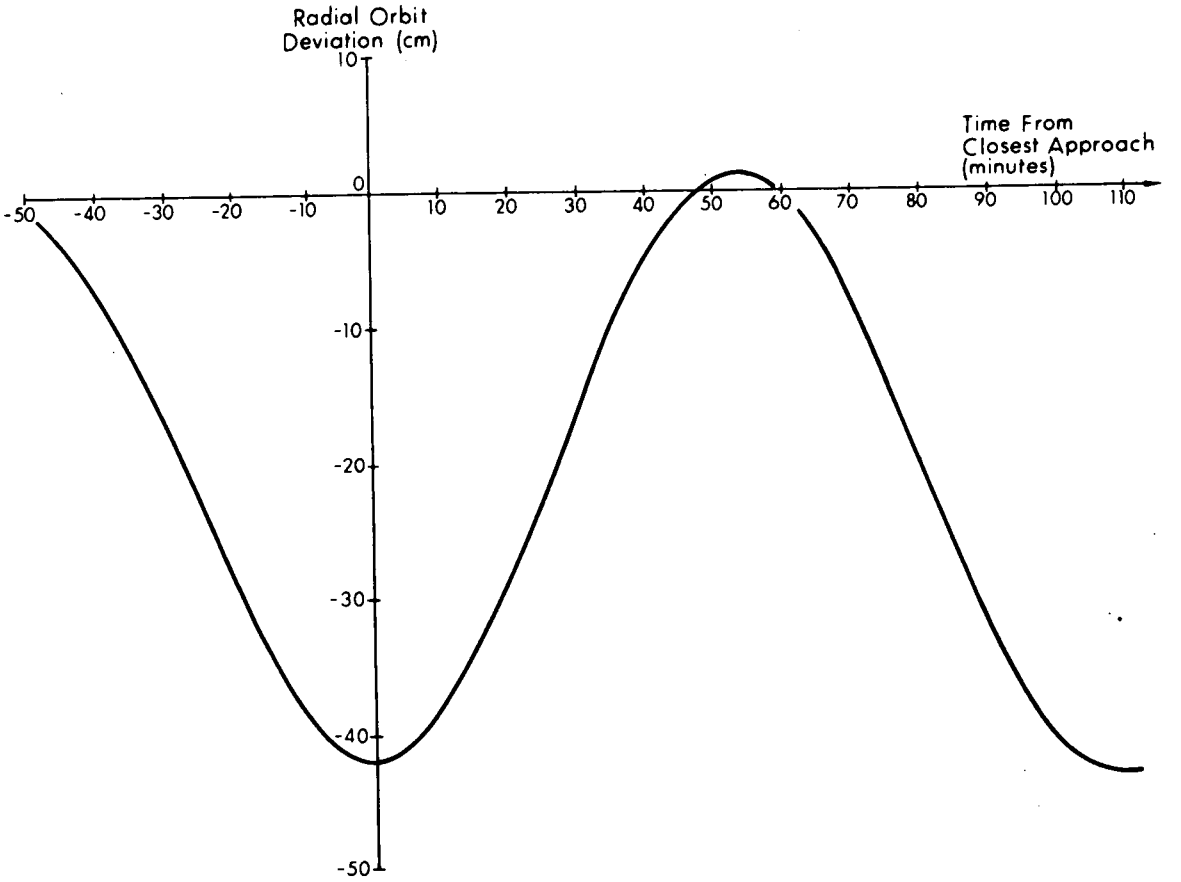

Figure 5-1. Effect of Mascon on GEOS-C Orbit

5.2 Hardware Errors

It is evident that any error in the altimeter measurement directly affects the accuracy of the determination of the geoid radius, inasmuch as the geoid radius is calculated from the altimeter measurement. Table 5-2 lists the factors that cause altimeter measurement error in excess of 10 cm. These factors are dependent on many parameters and can cause a wide range of error values. Typical expected values for these factors are presented in Table 5-2.

Table 5-2

Altimeter Measurement Corrections

SOURCE	TYPICAL MAGNITUDE CORRECTION NEEDED
ALTITUDE RATE	30 CM Note 1
ANTENNA OFFSET	1.5 M Note 2
SPACECRAFT LIBRATION	600 M Note 3
TRACKING LOOP NOISE	75 CM (Ref. 17)
CLOCK INSTABILITY	10 CM (Ref. 17)
CALIBRATION ERROR	1.2 M Note 4
ALTIMETER DRIFT	30 CM Note 5
REFRACTION	25 CM (eqn 5-8)
REFLECTIVITY	60 CM (Ref. 19)

Note: 1. From consideration of orbit ellipticity ($e < 0.006$), geoid slopes (Section 3.3) and a pulse rate of 6 per minute.

2. From geometrical considerations (eqn. 5-5) at 1.4° offset angle.

3. From geometrical considerations only (eqn. 5-5) at 3.3° libration angle.

4. Assuming a 4 nsec receiver delay time.

5. From equation 5-7 for assumed drift rate of 3cm per 100 hours of operating time and an operating time interval of 1000 hours.

Altitude rate is analogous to the dynamic tracking lag discussed in subsection 5.1. It is due to the time rate of change of altitude of the satellite and the finite time lag between transmission and return of the altimeter pulse. The error in altimeter reading due to altitude rate may be modeled as

$$\Delta h_a = \ddot{h}\mathcal{L} = \frac{\dot{h}_{i+1} - \dot{h}_i}{t_{i+1} - t_i}\ \mathcal{L} \qquad (5\text{-}4)$$

where $\ddot{h}$ = the time rate of change of altitude rate

$\dot{h}_i$ = the altitude rate at time t_i

$\mathcal{L}$ = the undetermined coefficient of the error model (sec^2)

Antenna offset refers to the misalignment of the antenna beam axis and the spacecraft stabilized axis. If the antenna is offset from the stabilization axis by an amount larger than the effective angular beamwidth, then the radar return to the spacecraft will not originate from the closest surface point to the satellite, but from some point whose distance is greater than the altitude. The altitude error due to this gross offset depends on the beamwidth half angle and the offset angle, and may be expressed for offset less than 5° from simple geometry by

$$\Delta h_o = H \tan\left(\frac{a_o - \delta_b}{2}\right) \tan(a_o - \delta_b) \text{ for } a_o \geqslant \delta_b. \qquad (5\text{-}5)$$

where a_o = the offset angle

δ_b = the beam half angle

H = the nominal altitude

Note: this formulation assumes that sufficient signal strength exists at high libration angles for normal operation of the altimeter signal detector.

Even when the offset is not enough to cause the closest point on the sea surface to fall outside the beam pattern, another type of antenna offset error is significant. This is the unequal distribution of transmitted radar signal around the measurement point that occurs when the measurement point lies off of the beam pattern symmetry axis. The absolute magnitude of the signal strength at this off-axis point is also generally different from the strength on-axis, thus causing errors in leading edge detection (Reference 17). At the present time, not enough is known about the design details of the altimeter to warrant an explicit error model for this comparatively minor antenna offset effect.

Spacecraft libration can cause errors whose characteristics are similar to those described above as antenna offset errors. In this case, the satellite attitude is offset from the desired stabilization direction due to orbit eccentricity, thermal effects, or solar wind (Reference 14). The offset is usually periodic in nature with a frequency equal to that of the satellite revolution about the earth. Replacement of the angle a_o in Equation (4-24) by

$$\alpha_\ell = A_\ell \sin (\omega_o t + \phi_\ell) \tag{5-6}$$

where a_ℓ = the spacecraft libration angle

A_ℓ = libration model coefficient

ω_o = the orbital angular rate

t = time from satellite epoch

ϕ_ℓ = the libration phase angle

yields a satisfactory error model for libration effects.

The altimeter is subject to many sources of error inherent in the electronic equipment (Reference 17). The exact error models developed to correct for these errors must await the design and development of the actual altimeter. Some of the more important sources are instrument delay, thermal noise, tracking loop jitter, clock instability, instrument delay variations, and data readout ambiguity (Reference 17). Instrument delay contributes a bias to the measurement and is included in Table 5-2 as calibration error.

Clock instability is a random error due to short-term drift instability in the altimeter's internal clock. The remainder of the instrument error sources contribute random errors and are lumped together as tracking loop noise in Table 5-2.

Altimeter drift is an error that is linear with time. Caused by such effects as electronic component aging, it is modeled by

$$\Delta h_D = D(t - t_o) \tag{5-7}$$

where D = the undetermined error model coefficient

$t-t_o$ = the time interval from present time t to initial time t_o

Atmospheric refraction also affects the altimeter measurement, although not as much as it does the tracking measurements. The vertical altimeter signal path through the atmosphere traverses less air mass and is not subject to bending. Hopfield's recent tropospheric refraction model (Reference 18), developed for Doppler measurement correction, has been adopted for correction of the altimeter measurement. Hopfield's model, with vertical incidence of the altimeter signal on the surface, reduces to

$$\Delta h_n = 2 \times 10^{-5} \left[N_{Td} \, (43.13 - 5.206 \sin^2 \phi) + 12 \, N_{Tw} \right] \quad (5\text{-}8)$$

where N_{Td} and N_{Tw} = refraction coefficients for the dry and wet components of the atmosphere ($N_{Td} = 265$ and $N_{Tw} = 110$ in mid-latitude marine summers).

ϕ = geographic latitude

Variations in reflectivity of the sea surface within the illuminated altimeter footprint can cause a distortion of the altimeter return pulse with consequent altimeter error. Pierson and Mehr (Reference 19) have found that the altimeter bias caused by the variation of reflection statistics with wave height can amount to tens of centimeters. The model describing the effect of reflection statistics on altimeter error requires knowledge of the transmitted pulse shape and detector design. Implementation of this model for evaluating and correcting surface reflectivity error must await a firm altimeter design.

5.3 Sea-Surface Errors

The instantaneous sea surface generally lies within a meter or two of the geoid (Reference 3), but such deviations cannot be neglected if an altimeter accuracy of 1 m or less is desired. The altitude measurement represents the shortest distance between the satellite and the sea surface. The deviation of the sea surface from the geoid is denoted δh_s and is defined along the ellipsoid normal (see Figure 4-1). Phenomena that can cause δh_s to be 10 cm or larger are listed in Table 5-3.

Referring to Table 5-3, swell describes long-wavelength water waves of the sort that propagate thousands of miles from the storm that spawned them. They typically have a sinusoidal shape, a wavelength of 200 m to 2 km, and propagate principally in one direction. Wind waves differ from swell in that they are shorter in wave-length, not obviously directional, and of irregular shape. Usually associated with strong winds, they have wavelengths from 1 cm to 300 m. Strong winds sometimes pile up water against the coast causing a local rise in the sea surface.

Table 5-3

Sea Surface — Geoid Deviation Sources

SOURCE	TYPICAL MAGNITUDE[1]
SEA SWELL	1 M
WIND WAVES	1 M
STORM SURGE	10 CM
BAROTROPIC DEPRESSIONS	10 CM
CURRENTS	1 M
TIDES	1 M

[1]REFERENCE 3.

This effect is called storm surge. Barotropic depressions caused by high- and low-pressure areas of global weather patterns result in a local sea-surface deviation from the geoid.

Ocean currents can cause local sea-surface deviations due to the coriolis effect. Consequently, the observed surface deflection, with a maximum at the maximum velocity point, is greatest in the higher latitudes and for East-West currents.

Tides, so well measured near the coasts of continents, are nearly undetermined in midocean. Theories for the time-dependent sea-surface deviations due to tides have been developed (Reference 3) and the frequencies of the various tidal components are known. A localized time-dependent, tidal deflection error model has been developed for the component frequencies whose amplitudes are dominant (Reference 20). Accordingly, the expected tidal surface deviation at latitude Φ (in degrees), longitude λ (in degrees), and mean solar time (at Greenwich in hours), t, is

$$\Delta h_T = 0.2667 \left\{ \frac{1}{2} (1-3 \sin^2 \Phi) \left[A_t + M_f \cos (1.098t + 41.2) \right] \right.$$

$$+ \sin 2\Phi \left[OK_1 \cos (15.041t + 65 + \lambda) \right] \qquad (5\text{-}9)$$

$$\left. + \cos^2 \Phi \left[M_2 \cos (28.984t + 135 + 2\lambda) \right] \right\} \text{(meters)}$$

where A_t, M_f, OK_1, and M_2 are coefficients to be adjusted.

This model was developed from the known dominant monthly, daily, and half-daily tidal components, aggregating components of common periods by choosing an average phase angle.

The other sea-surface effects mentioned above may be modeled by a local sea-level bias.

5.4 Simulation Results

The effect on the predicted satellite position of bias in the satellite tracking measurement has been partially evaluated in a computer simulation. The NAP program was used to simulate biased and noisy C-band radar tracking data for a typical GEOS-C orbit. The NAP program simulates the tracking data and computes a least-squares differential correction to the GEOS-C state vector. This adjusted state vector represents the best estimate of the satellite state vector given the erroneous tracking data. The difference between the radial components of the satellite position vectors predicted by the simulated data and by the uncorrupted data (represented by the nominal or a priori state vector) is evaluated and plotted in the NONAME Program (RV compare option). This vector component difference represents the error in calculated altitude due to the biased tracking data.

To date one simulation has been carried out: for a 6-hour orbital arc with perturbed tracking data from eight C-band tracking sites. The a priori measurement bias was 6 m with a standard deviation of 3 m, which is the expected range bias uncertainty in accordance with officially documented tracking system performance (Reference 21). The stations tracking GEOS-C were assumed to be located at:

Kauai, Hawaii
Pt. Mugu, California
White Sands, New Mexico
Eglin AFB, Florida
Cape Kennedy, Florida
Grand Bahama Island, Bahama Islands
Antigua Island, Lesser Antilles
Pretoria, South Africa

The elevation limits imposed precluded tracking below 5 degrees elevation for these stations. The average pass length was 15 minutes, and the 6-hour arc length allowed about two consecutive passes per station. The gravity field model used was the SAO-M1 field.

Simulated data were generated every 5 minutes during the visibility period for each station. The resulting predicted orbit deviates from the nominal (error free) orbit and the radial deviations are plotted in Figure 5-2.

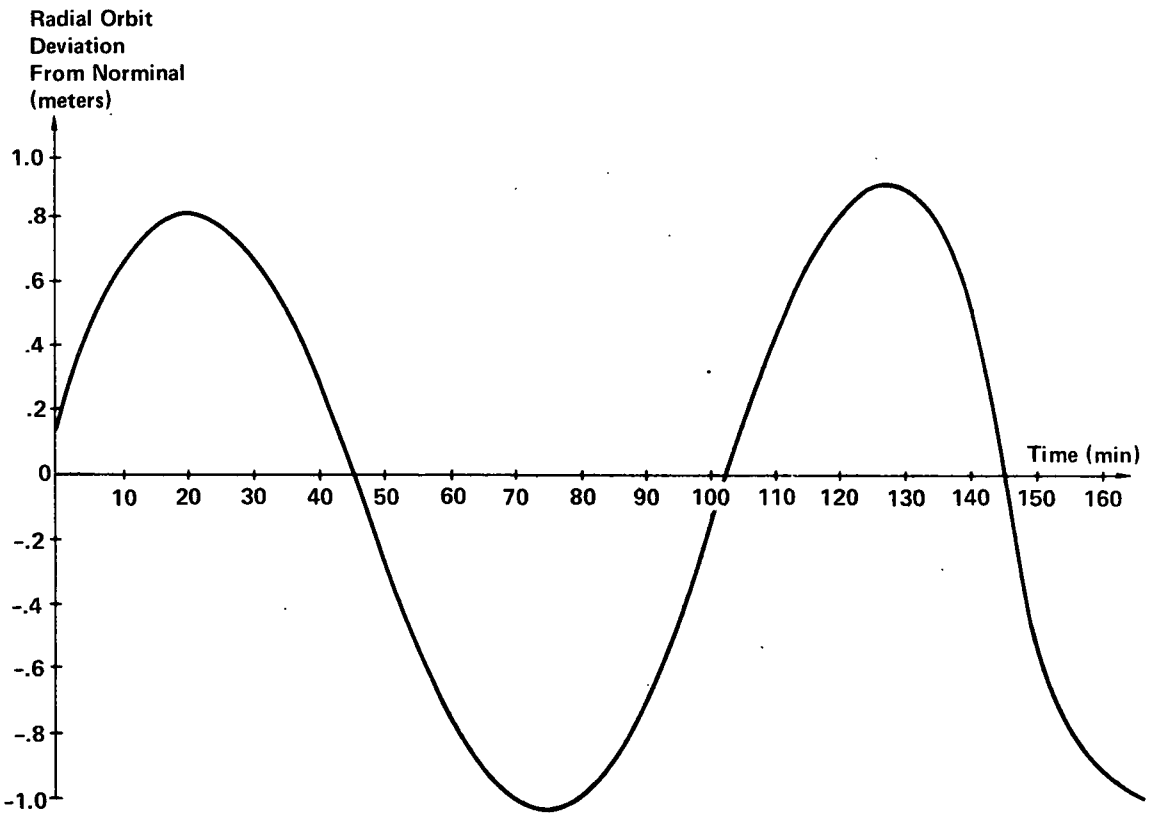

Figure 5-2. Radial Orbit Deviations Due to Biased C-Band Range Data

The maximum radial deviation, or altitude error, due to tracking system bias in this case is about 1 m. This is the magnitude of the error in the altitude calculation due to bias and noise in C-band tracking for the situation tested. The altitude error is expected to vary as data rate, station distribution, and tracking duty cycle are changed.

APPENDIX A

SAMPLE DIFFERENTIAL CORRECTION PROCEDURE

The following discussion is provided as an example of the differential correction procedure that might be used in processing altimeter data. This procedure involves the formation of the difference (residual) between the observed and calculated (expected) altitudes and the solution for differential corrections to the parameters of the problem, such that the weighted sum of the squares of the residuals is minimized.

The residuals are formed using the difference between the expected and the observed altitude measurements. The observed altitude is the altitude measurement at time t_r, denoted O_r. The expected altitude to the sea surface may be obtained from Equation (4-20). To this must be added certain error models that enable one to express the expected altitude measurement. In functional form, the expected altitude measurement function is

$$\mathcal{H} = h\ (\vec{E}_o,\ t) - N(\vec{G}_o) - \delta h_s\ (\vec{\tau}_o,\ \vec{S}_o,\ \phi,\ \lambda,\ t) - \Delta h\ (\vec{m}_o,\ \phi,\ t) \quad \text{(A-1)}$$

where h = the calculated altitude to the reference ellipsoid

$\vec{E}_o$ = the vector of orbital elements, and other arc-dependent parameters, such as drag and solar pressure

t = time

$\vec{G}_o$ = a vector of geopotential coefficients

N = the geoid undulation function

δh_s = the sea-surface deviation function

$\vec{\tau}_o$ = a vector of tidal error model coefficients

$\vec{S}_o$ = a vector of local sea-surface biases

ϕ = the geodetic latitude of the altimeter measurement point

λ = the longitude of the altimeter measurement point

Δh = the functional representation of altimeter measurement errors

$\vec{m}_o$ = a vector of altimeter measurement error coefficients

Written in this form, Equation (A-1) is not the best estimate of the true altitude at time t but is the best estimate of the actual altitude measurement, as affected by altimeter error sources. Note that for simplicity the expected

altitude to the ellipsoid, h, is not here expressed as a function of geopotential coefficients, $\vec{G}_o$. The measurement residual is

$$(O - \mathcal{H})_r$$

where r denotes the r^{th} measurement.

Mathematically, this residual is equivalent to the difference function,

$$\Delta\mathcal{H}_r = \sum_{h=1}^{8} \frac{\partial \mathcal{H}}{\partial E_h}\bigg|_r dE_h + \sum_{k=1}^{L} \frac{\partial \mathcal{H}}{\partial G_k}\bigg|_r dG_k + \sum_{i=1}^{5} \frac{\partial \mathcal{H}}{\partial \tau_i}\bigg|_r d\tau_i + \sum_{j=1}^{q} \frac{\partial \mathcal{H}}{\partial S_j}\bigg|_r dS_j + \sum_{i=1}^{p} \frac{\partial \mathcal{H}}{\partial m_i}\bigg|_r dm_i + \vec{\delta}_o \tag{A-2}$$

where L, q, and p are the total number of geopotential, sea-surface bias, and altimeter measurement error model coefficients, respectively. In matrix form, Equation (A-2) is

$$\overrightarrow{(O - \mathcal{H})} = [A_o]\,\vec{dE} + [C_o]\,\vec{dG} + [F_o]\,\vec{d\tau} + [K_o]\,\vec{dS} + [L_o]\,\vec{dm} + \vec{\delta}_o \tag{A-3}$$

where $\vec{\delta}_o$ is the N-dimensional vector of unmodeled errors between O and $\mathcal{H}$ for the N measurements, r = 1, 2, . . ., N.

To this observation equation we add the observation equation of the additional satellite tracking data available from satellite-to-satellite tracking and various ground-based tracking systems, such as laser, C-band, and Doppler,

$$\overrightarrow{(O' - M)} = [Q]\,\vec{dE} + \vec{\delta}'_o \tag{A-4}$$

The resulting observation equation may be further reduced in matrix notation to

$$\vec{R} = [M]\,\vec{Z} + \vec{\delta}_1 \tag{A-5}$$

where

$$\vec{R} = \begin{pmatrix} (O_1 - \not{H}_1) \\ (O_2 - \not{H}_2) \\ \cdot \\ \cdot \\ \cdot \\ (O_N - \not{H}_N) \\ \dot{(O' - M)} \end{pmatrix} \qquad \vec{Z} = \begin{pmatrix} \vec{dE} \\ \vec{dG} \\ \vec{d\tau} \\ \vec{dS} \\ \vec{dm} \end{pmatrix}$$

and

$$[M] = \begin{bmatrix} \vec{A}_o & \vec{C}_o & \vec{F}_o & \vec{K}_o & \vec{L}_o \\ \vec{Q} & 0 & 0 & 0 & 0 \end{bmatrix}$$

For a least-squares solution, we seek a vector $\vec{Z}$ such that

$$\vec{\delta}_1^T [G] \vec{\delta}_1 = \text{MIN} \tag{A-6}$$

where [G] = the inverse variance/covariance matrix of the observations; that is, the weighted square of the unmodeled error, is minimized.

These measurements are usually assumed to be uncorrelated so that $G_{ij} = 0$, $i \neq j$, and the measurement weight matrix [G] is diagonal.

The minimization of $\vec{\delta}_1^T$ [G] $\vec{\delta}_1$ is accomplished by the solution of the normal equation

$$[M]^T [G] [M] \vec{Z} = [M]^T [G] \vec{R} \tag{A-7}$$

Equation (A-7) is solved for the differential corrections Z, which are then applied to the error models coefficients and force model parameters. The expected altitude measurement $\not{H}$ is recalculated based on these improved coefficients and parameters, and a new residual vector $\vec{R}$, is calculated. Equation (A-7) is solved again, if necessary, and each iteration reduces the residuals $\vec{R}$ until they and the calculated differential correction are small enough that the parameter vectors in Equation (A-1) can be said to have converged.

The direct solution of Equation (A-7) is straightforward but not always desirable. It may happen that the a priori parameter values used in forming

the matrix M are so different from their converged values that Equation (A-7) will not lead to a converging solution. If this is the case, and if the normal equation matrix $[M]^T$ [G] [M] is such that off-diagonal elements common to different subsets of parameters are small compared with the diagonal elements, then the parameter set $\vec{Z}$, and the normal equation matrix may be divided into subsets to be solved separately. Thus an improved set of values for parameter subset 1 may be obtained for use in solving for parameter subset 2, and so on, until a complete set of starting elements for solving Equation (A-7) is obtained. Of course, if the off-diagonal elements of $[M]^T$ [G] [M] are zero for a given subset of parameters, then that subset of parameters may be solved completely independently of the other subsets.

This technique is currently used in processing satellite tracking data wherein orbit parameters are adjusted and converged separately and only one iteration thereafter is necessary to obtain good geopotential coefficient adjustments. A similar situation may exist in the case of altimeter data processing. The orbit parameters and geopotential coefficients should have small off-diagonal elements in common in the normal equation matrix. Similarly, sea-surface deviation parameters are relatively independent of the other parameters. On the other hand, altimeter measurement error parameters are closely related to orbit parameters in their effect on measurement residuals. Therefore, solution of $\vec{dE}$ and $\vec{dm}$ (hereafter called the orbit subset), separately from $\vec{d_T}$ and $\vec{dS}$ (the surface subset), and from $\vec{dG}$, should be fruitful.

This particular partition of altimeter parameters is also desirable because of the different characteristics of these parameters. The orbit is best solved for using time-ordered sequences of data such as tracking station passes and altimeter turn-on periods, which are independent of geographical area. The surface subset, because of the localized nature of the sea-surface deviation phenomena, is best solved for using the measurements that fall in the localized area in question.

Solving first for the orbit subset, Equations (A-3) and (A-4) may be written as

$$\begin{bmatrix} \overrightarrow{(O - \mathcal{H})} \\ \hline \overrightarrow{(O' - M)} \end{bmatrix} = \begin{bmatrix} A_o & L_o \\ \hline Q & 0 \end{bmatrix} \begin{bmatrix} \vec{dE} \\ \hline \vec{dm} \end{bmatrix} + \begin{bmatrix} \vec{\delta}_o \\ \hline \vec{\delta}'_o \end{bmatrix} \qquad \text{(A-8)}$$

or

$$\vec{R} = [M]_o \begin{bmatrix} \vec{dE} \\ \hline \vec{dm} \end{bmatrix} + \vec{\delta}_1 \qquad \text{(A-9)}$$

where the subscript o indicates orbit subset. The corresponding normal equation solution for the orbit subset of parameter adjustments is

$$\begin{pmatrix} d\vec{E} \\ \hline d\vec{m} \end{pmatrix} = \left[[M]_o^T [G] [M]_o \right]^{-1} [M]_o^T [G] \vec{R} \qquad \text{(A-10)}$$

The updated orbit subset parameters are

$$\vec{E}_1 = \vec{E}_o + d\vec{E} \qquad \text{(A-11)}$$

$$\vec{m}_1 = \vec{m}_o + d\vec{m} \qquad \text{(A-12)}$$

At this time, the altimeter residuals may be processed through a high-pass filter to remove the low-frequency radial orbit perturbation contributed by low-order and degree geopotential terms. The altimeter residuals now contain high-frequency geoid undulations contaminated by sea-surface deviations and leftover uncorrected errors in the orbit subset.

The relevant equations for solution of these orbit and sea-surface effects are as follows:

$$\mathcal{H}_I = h''(\vec{E}_1, \vec{G}_o, t) - N(\vec{G}_o) - \delta h_s(\vec{\tau}_o, \vec{S}_o, \phi, \lambda, t) - \Delta h(\vec{m}_1, \phi, t) \qquad \text{(A-13)}$$

$$(O - \mathcal{H}_I) = [F_o] d\vec{\tau} + [K_o] d\vec{S} + [A_1] d\vec{E} + [L_1] d\vec{m} + \vec{\delta}_2 \qquad \text{(A-14)}$$

$$\begin{pmatrix} d\vec{E} \\ d\vec{m} \\ d\vec{\tau} \\ d\vec{S} \end{pmatrix} = \left[[M]_{os}^T [G] [M]_{os} \right]^{-1} [M]_{os}^T [G] \vec{R}_I \qquad \text{(A-15)}$$

and

$$\begin{aligned} \vec{E}_2 &= \vec{E}_1 + d\vec{E} \\ \vec{m}_2 &= \vec{m}_1 + d\vec{m} \\ \vec{\tau}_1 &= \vec{\tau}_o + d\vec{\tau} \\ \vec{S}_1 &= \vec{S}_o + d\vec{S} \end{aligned} \qquad \text{(A-16)}$$

where the subscript os indicates the orbit and sea-surface subsets and $[A_1]$ and $[L_1]$ are the updated submatrices of partials for the orbit subset of parameters.

The residuals that remain after the expected altitude measurement $\mathcal{H}$ is recalculated contain geoid undulations and uncorrected orbit and sea-surface effects. Equations (A-3) through (A-7) may be updated and summarized:

$$\mathcal{H}_{II} = h''(\vec{E}_2, \vec{G}_o, t) - N(\vec{G}_o) - \delta h_s(\vec{\tau}_1, \vec{S}_1, \phi, \lambda, t) - \Delta h(\vec{m}_1, \phi, t) \quad \text{(A-17)}$$

$$\overrightarrow{(O - \mathcal{H}_{II})} = [C_o]d\vec{G} + [A_2]d\vec{E} + [L_2]d\vec{m} + [F_1]d\vec{\tau} + [K_1]d\vec{S} + \vec{\delta}_3 \quad \text{(A-18)}$$

$$\vec{Z} = \left[[M]_1{}^T[G][M]_1\right]^{-1}[M]_1^T[G]\vec{R}_{II} \quad \text{(A-19)}$$

where the subscripts on matrices and vectors reflect the updating of the parameters through previous subset solutions.

APPENDIX B

GEOPOTENTIAL MODELS

Several different mathematical models of the geopotential have been examined for use in the altimeter data processing simulation. These models and their relation to the calculated altitude measurement are presented below.

B. 1 Spherical Harmonic Expansion

In this model, the disturbing potential T is written as

$$T(r, \phi, \lambda) = \frac{GM}{r} \left[\sum_{n=2}^{L^*} \sum_{m=0}^{n} \left(\frac{a}{r}\right)^n (C_{nm} \cos m\lambda + S_{nm} \sin m\lambda) P_n^m (\sin \phi) \right] \quad \text{(B-1)}$$

The relation between T and the calculated altitude measurement $\mathcal{H}$ is expressed, using Brun's formula (Equation (3-5)) as

$$\mathcal{H} = h - \frac{T}{\gamma}(C_{nm}, S_{nm}) - \delta h_s - \Delta h \quad \text{(B-2)}$$

The appropriate partial derivatives in the altitude measurement condition equation (see Appendix A) are

$$\left[C_{o_{kl}}\right] = \begin{bmatrix} \frac{\partial \mathcal{H}_1}{\partial C_{20}} & \frac{\partial \mathcal{H}_1}{\partial C_{30}} & \cdots & \frac{\partial \mathcal{H}_1}{\partial S_{nm}} \\ \vdots & & & \\ \frac{\partial \mathcal{H}_N}{\partial C_{20}} & \frac{\partial \mathcal{H}_N}{\partial C_{30}} & \cdots & \frac{\partial \mathcal{H}_N}{\partial S_{nm}} \end{bmatrix} \quad \text{(B-3)}$$

where

$$\frac{\partial \mathcal{H}}{\partial C_{nm}} = \frac{\partial N}{\partial C_{nm}} = \frac{GM}{r}\left(\frac{a}{r}\right)^n \cos m\lambda \, P_n^m (\sin \phi') \quad \text{(B-4)}$$

and

$$\frac{\partial \mathcal{H}}{\partial S_{nm}} = \frac{\partial N}{\partial S_{nm}} = \frac{GM}{r}\left(\frac{a}{r}\right)^n \sin m\lambda \, P_n^m (\sin \phi')$$

B.2 Local (Sample) Function Model

In this model, the disturbance potential is expressed in terms of sample functions that are nonzero only in certain geographic areas.

$$T(r, \phi, \lambda) = GM \sum_{j=1}^{L} G_j \, \gamma_j (r, \phi, \lambda) \tag{B-5}$$

where $\gamma_j(r, \phi, \lambda)$ are the sample functions (Reference 4).

The calculated altitude measurement is written as

$$\mathcal{H} = h - \frac{T}{\gamma}(\vec{G}) - \delta h_s - \Delta h \tag{B-6}$$

and the conditions equation partial derivatives become

$$C_{o_{k\ell}} = \frac{\partial \mathcal{H}_k}{\partial G_\ell} = \frac{1}{\gamma}\frac{\partial T}{\partial G_\ell} = \frac{GM}{\gamma}\gamma_\ell (r, \phi, \lambda) \tag{B-7}$$

where $C_{o_{k\ell}} = 0$ unless the k^{th} observation lies in the ℓ^{th} geographic area.

B.3 Surface Layer Model

This model presents the disturbing potential as due to a thin layer of material of varying density G_i deposited on the reference surface (Reference 22). The disturbing potential is expressed as

$$T(r, \phi, \lambda) = \sum_{i=1}^{L} G_i \iint_{\Delta\sigma_i} \frac{d\sigma}{\ell_i} \tag{B-8}$$

where $\Delta\sigma_i$ = the i^{th} finite surface element

ℓ_i = the distance between the point (r, ϕ, λ) and the centroid of the i^{th} surface element

The calculated altitude measurement is given by Equation (B-6) and the condition equation partial derivatives are

$$C_{o_{k\ell}} = \frac{\partial \mathcal{H}_k}{\partial G_\ell} = \frac{1}{\gamma}\frac{\partial T}{\partial G_\ell} = \frac{1}{\gamma}\iint \frac{d\sigma}{\ell_\ell} \qquad \text{(B-9)}$$

Vinti (Reference 23) also describes a surface layer model.

B.4 Free-Air Gravity Anomaly Model

This model (Reference 24 and 11) express the disturbing potential at a given point P (r, ϕ, λ) by a sum of gravity anomalies in a small area around P. The disturbing potential is written as

$$T(r, \phi, \lambda) = T_1(r, \phi, \lambda) + \sum_{j=1}^{L} \overline{\Delta g}\,(\phi_j, \lambda_j)\, S(\Psi)\, \Delta\sigma_j \qquad \text{(B-10)}$$

where T_1 = the disturbing potential calculated by a set of low-order and degree spherical harmonics which are not adjusted

$\overline{\Delta g(\phi_j, \lambda_j)}$ = the mean free-air gravity anomaly referenced to the equipotential surface of T_1 in the j^{th} element of area

Ψ = the angular arc between (ϕ, λ) and (ϕ_j, λ_j)

$S(\Psi)$ = Stokes' function

$\Delta\sigma_j$ = the size of the elemental areas

The calculated altitude measurement is given by

$$\mathcal{H}(P) = h\ (P) - \frac{T}{\gamma}(\vec{G}) - \delta h_s\ (P) - \Delta h \qquad \text{(B-11)}$$

where

$$\vec{G} = \begin{pmatrix} \overline{\Delta g}\ (\phi_1, \lambda_1) \\ \vdots \\ \overline{\Delta g}\ (\phi_j, \lambda_j) \\ \vdots \\ \overline{\Delta g}\ (\phi_L, \lambda_L) \end{pmatrix} \tag{B-12}$$

and the corresponding condition equation partial derivatives are

$$C_{o_{k\ell}} = \frac{1}{\gamma} S(\Psi_\ell)\, \Delta\sigma_\ell \tag{B-13}$$

GLOSSARY OF SYMBOLS

Symbol	Definition
$[A_o]$	Matrix of orbital element partial derivatives
A_ℓ	Libration coefficient
A_t	Tidal model coefficient
a	Semimajor axis of the reference ellipsoid
α	Angle between the local vertical at p and the x-axis of the geodetic coordinate system
α_ℓ	Satellite libration angle
α_o	Antenna offset angle
B	Measurement bias
B_E	Coefficient of tracking station error
B_N	Coefficient of tracking station error
B_U	Coefficient of tracking station error
b	Semiminor axis of reference ellipse
β	Angle between the local vertical at p and the y-axis of the geodetic coordinate system
$\left[C_{o_{k\ell}}\right]$	Matrix of geopotential coefficient partial derivatives
c	Speed of light (kilometers per second)
γ	Angle between the local vertical at p and the z-axis of the geodetic coordinate system
γ_Q	Gradient of U at Q
Ω	Phase error
D	Altimeter drift error coefficient

Symbol	Definition
$\overrightarrow{\Delta g}$	Mean free air gravity anomaly
Δh_a	Altitude correction due to altitude rate
Δh_D	Altimeter drift error
Δh_o	Antenna offset altitude correction
Δh_n	Tropospheric refraction altitude correction
Δh_T	Tidal altitude correction
$\Delta\rho$	Range error due to refraction
$\Delta\rho_{rf}$	Specific ionospheric refraction correction
δb	Half angle of altimeter beamwidth
δh_s	Sea-surface deviation from the geoid along reference ellipsoid normal at Q
$\delta h_{s'}$	Sea-surface deviation from the geoid at S' (acceleration of normal gravity)
$\vec{\delta}_o, \vec{\delta}_1, \vec{\delta}_2$	Vector of unmodeled errors
$\delta\rho$	Correction to range measurement due to error source
$\Delta\sigma_j$	Incremental surface element
$\vec{E}_o$	Vector of orbital and arc-dependent elements
E	Elevation angle of ray path from tracking station to satellite
ϵ	Angular difference between geoid and ellipsoid normals (deflection of the vertical)
$[F_o]$	Matrix of tidal model partial derivatives
f	Flattening of the reference ellipsoid

Symbol	Definition
[G]	Inverse variance/covariance matrix
GM	Gravitational constant of the earth
$\vec{G}$	Vector of geopotential coefficients
$\vec{g}$	Gravity acceleration vector (local vertical) at the satellite
$\mathcal{H}$	Expected altitude measurement
H	Nominal satellite altitude (km)
H′	Satellite altitude above the geoid along $\hat{n}$ at S′
H″	Approximation to H at P
h′	Altitude of the satellite above the reference ellipsoid at S′
h	Approximation to the satellite altitude above the reference ellipsoid at P
h_1, h_i	Successive approximations to h
$\dot{h}_i$	Time rate of change of altitude at time t_i
$\ddot{h}$	Time rate of change of altitude rate
η	Component of the deflection of the vertical
$[K_o]$	Matrix of local sea-surface partial derivatives
$[L_o]$	Matrix of altimeter error model partial derivatives
$\mathcal{L}$	Altitude rate error coefficient
L;L*	Range dynamic lag; number of geopotential coefficients
λ	Longitude
$[M_o]$	Matrix of parameter partial derivatives

Symbol	Definition
$\vec{M}$	Measurement vector of "other" data type
M_f	Tidal model coefficient
M_2	Tidal model coefficient
$\vec{m}$	Vector of altimeter measurement error coefficients
m	Order of spherical harmonic term
N	Geoid undulation (meters)
N'	Geoid undulation at S'
N_{T_d}, N_{T_W}	Dry and wet refractivity coefficients, respectively
n	Degree of spherical harmonic term
$\hat{n}'$	Unit vector along the ellipsoid normal
n_s	Index of refraction
ξ	Component of the deflection of the vertical
O_r	Observed altitude at time t_r
OK_1	Tidal model coefficient
P	Observation point on the geoid surface
p	Number of altimeter measurement error coefficients
Q	Point on the reference ellipsoid obtained by projection from P along the ellipsoid normal at P
q	Number of local sea-surface bias coefficients
$\vec{R}$	Vector of altimeter residuals
R	Coefficient of ionospheric refraction
R_S	Effective illuminated surface spot radius (km)

Symbol	Definition
r	Geocentric radius to P
r_e	Geocentric radius of the satellite
r_N	Normal meridional radius of curvature at S'
r_{N_1}	First approximation to r
r_s	Geocentric radius to tracking station
r_{se}	Geocentric radius to point S' on the reference ellipsoid
ρ	Range from tracking station to satellite
$\dot{\rho}$	Time rate of change of range
$\rho_{x_s}, \rho_{y_s}, \rho_{z_s}$	Partial derivative of range with respect to parameters μ
S	Range scale-length error
$S(\Psi)$	Stokes' function
S'	Satellite subpoint on the reference ellipsoid
$\vec{S}_o$	Vector of local sea-surface biases
T	Disturbing potential function; timing bias
T_1	Disturbing potential function
t	Time
τ	Transmitted radar pulsewidth (seconds); specific phase error
$\vec{\tau}_o$	Vector of tidal error model coefficients
U	Normal potential function
Φ	Geodetic latitide of point Q
Φ^*	Astronomical latitude of P

Symbol	Definition
ϕ	Geodetic latitude of the point S'
ϕ_1, ϕ_2, ϕ_i	Successive approximations to ϕ
ϕ	Geocentric latitude of S'
ϕ_ℓ	Libration phase angle
W	Geopotential function
X, Y, Z	Coordinates of the observation point P on the geoid surface
γ	Local (sample) Function
X_e, Y_e, Z_e	Earth-fixed coordinates of the satellite
X_s, Y_s, Z_s	Tracking station error parameters
$\vec{Z}$	Vector of differential corrections
Ψ	Geodetic latitude of point Q; angular arc surface distance
Ω	Geodetic longtitude of point Q
Ω^*	Astronomical longtitude of P
ω_o	Satellite orbital rate

REFERENCES

1. Strange, W. E., "Marine Geodesy, "EOS, Transactions of the American Geophysical Union, March 1971, Vol. 52, No. 3.

2. Hudson, E. F., "Determining the Geometric Shape of the Geoid in Ocean-Covered Areas of the World by Satellite Radar Altimeter" (abstract), EOS, Transactions of the American Geophysical Union, 1970, Vol. 51, p. 263.

3. New York University School of Engineering and Science, Department of Meteorology and Oceanography, Report on Contract N62306-1589, U. S. Naval Oceanographic Office, Radar Altimetry from a Spacecraft and its Potential Applications to Geodesy and Oceanography, J. A. Greenwood, et al., May 1967.

4. Smithsonian Astrophysical Observatory, Report No. 294, Possible Geopotential Improvement from Satellite Altimetry, C. A. Lundquist, G. E. O. Giacaglia, K. Hebb, and S. G. Mair, 1970.

5. MIT Measurement Systems Lab., RE-37, Combining Satellite Altimetry and Surface Gravimetry in Geodetic Determinations, R. G. E. Young, 1970.

6. Koch, K. R., "Gravity Anomalies for Ocean Areas from Satellite Altimetry," Proceedings of the Second Marine Geodesy Symposium, Marine Technology Society, Washington, D. C., 1970.

7. National Aeronautics and Space Administration, Goddard Space Flight Center, X-552-70-136, Tracking Accuracy Studies of GEOS-C Orbits for Altimetry Using Radar and Optical Data, J. G. Marsh and B. C. Douglas, February 1970 (preprint).

8. Computer Sciences Corporation, "Task Assignment #210, Determination of the Geoid from Satellite Altimeter Data, Memorandum of Understanding," R. D. Brown, Letter attachment from R. L. Taylor (CSC) to W. D. Kahn (NASA, GSFC), November 4, 1971.

9. Heiskanen, W. A., and H. Moritz, Physical Geodesy, W. H. Freeman and Co., 1967.

10. Smithsonian Astrophysical Observatory, Special Report No. 200, Geodetic Parameters for a 1966 Smithsonian Institution Standard Earth, Vol. 3, C. A. Lundquist and G. Veis, 1966.

11. Richardson, J. A., "Summary of Activities on Task 256, Computer Sciences Corp., Technical Memorandum 5035-25600-OITM Task Assignment 256, Contract No. NAS5-11790, June 1972.

12. Vincent, S., W. E. Strange, and J. G. Marsh, "A Detailed Gravimetric Geoid from North America to Europe" (paper presented at the National Fall Meeting, American Geophysical Union, San Francisco, California, December 6-9, 1971).

13. MIT Experimental Astronomy Laboratory, RE-48, Signal Processing in a Satellite Radar Altimeter, C. F. Price, August 1968.

14. Raytheon Co., Space Geodesy Altimetry Verification Experiment Design Study, Final Report, NASA Contract NASW-1920, E. Weiss, April 1970.

15. Kershner, R. B., and R. E. Fischell, "Gravity Gradient Stabilization of Earth Satellites," Johns Hopkins University Applied Physics Laboratory (paper presented at the International Federation of Automatic Control Symposium in the Peaceful Uses of Space, Stavanges, Norway, 1965).

16. Bomford, G., Geodesy, 2nd Edition. London: Oxford University Press, 1962.

17. National Aeronautics and Space Administration, Goddard Space Flight Center, Contracts NAS 5-10588 and NAS 5-11729, Mod. 1, Network Analysis Program - NAP-3, Mathematical Analysis Documentation, J. J. Lynn, J. G. Hartwell, and R. S. Nankervis, June 1, 1970.

18. National Aeronautics and Space Administration, Goddard Space Flight Center, Proposal for Sky Lab. Earth Resources Experimental Package Altimeter Evaluation and Analysis, J. W. Bryan, (unpublished).

19. Johns Hopkins University Applied Physics Laboratory, TG-1024, A Two-Quartic Refractivity Profile for the Troposphere, for Correcting Satellite Data, H. S. Hopfield, September 1968.

20. New York University School of Engineering and Science: Department of Meteorology and Oceanography, Spacecraft Oceanography Project, U. S. Naval Oceanographic Office, Contract N62306-70-A-0075, Task Order 0001, The Effects of Wind Waves and Swell on the Ranging Accuracy of a Radar Altimeter (Part I), W. J. Pierson and E. Mehr.

21. U. S. Department of Commerce, Coast and Geodetic Survey, Special Publication No. 98, Manual of Harmonic Analysis and Prediction of Tides, P. Shureman, 1958.

22. National Aeronautics and Space Administration, Goddard Space Flight Center, Document I-500-70-173, The 1975 Satellite Network, September 1970.

23. NOAA, Technical Memorandum NO59, The Earth's Gravity Field Represented by a Simple Layer Potential from Doppler Tracking of Satellites, K. R. Koch and B. V. Witte, April 1971.

24. Vinti, J. P., "Representation of the Earth's Gravitational Potential," Celestial Mechanics, December 1971, Vol. 4, No. 3/4.